frontiers in Earth Science

ORIGINAL RESEARCH
published: 21 May 2021
doi: 10.3389/feart.2021.657083

# Geochronology and Geochemistry of Late Paleozoic Volcanic Rocks and Their Relationship With Iron and Molybdenum Deposits in Xilekuduk Area, Northern Margin of Junggar

*Xiaofeng Wei[1], Hao Wei[2]*, Zhen Liao[3], Zhiwei Wang[2], Dong Li[2], Qigui Mao[4] and Xiao Li[2]*

*[1]Zhongse Zijin Geological Exploration (Beijing) Co., Ltd., Beijing, China, [2]Hebei Key Laboratory of Strategic Critical Mineral Resources, Hebei GEO University, Shijiazhuang, China, [3]Sinotech Minerals Exploration Co., Ltd., Beijing, China, [4]Beijing Institute of Mineral Geology Co., Ltd., Beijing, China*

A large number of intermediate basic volcanic rocks and porphyry Cu-Mo deposits as well as volcanic-hosted magnetite deposit have been recently discovered in the Xilekuduk area. However, no reports concerning petrogenesis and age or their relationship with mineralization have been published to date. The purpose of this study was to make up for the absence of previous studies on Devonian volcanic activities in the area and to confirm the relationship between two stages of volcanic activities and mineralization so as to provide important theoretical basis for mineral exploration. Based on research results of zircon U-Pb geochronology and element geochemistry of volcanic rocks in the area, the ages of dacite, andesite, and stomatal andesite are considered as 375.2 ± 2.9 Ma, 386.5 ± 3.0 Ma, and 317.9 ± 2.9 Ma, respectively, corresponding to the Middle Devonian and Late Carboniferous Period. The Devonian volcanic rocks belong to the high-K calc-alkaline series and island arc volcanic rocks, which are enriched in LREE, strongly enriched in large ion lithophile elements Th, Rb, Ba, and K and relatively depleted in high-field strength elements (HFSEs) Nb, Ta, and Ti. The Carboniferous volcanic rocks are enriched in LREE, as well as the large ion lithophile elements Th, Rb, Ba, and K are strongly enriched, while depleted in the HFSEs Nb, Ta, and Ti; moreover, the contents of $TiO_2$ and V are 0.94–0.97% and 178–183×$10^{-6}$, which are higher than those of island arc basalts. According to mineralogical typomorphic characteristics and geochemical analysis, magnetite mineralization is divided into two phases. The early stratiform magnetite ore MT1 has magmatic characteristics, forming a volcanic rock type magnetite deposit related to Devonian volcanic eruption and sedimentation (375–386 Ma). The magnetite MT2 in the magnetite-quartz vein is considered as hydrothermal genesis, which is a metal mineral in the early metallogenic stage of Carboniferous (317.1 ± 2.9 Ma) volcanic eruption and subvolcanism, and may be related to porphyry molybdenum mineralization. Therefore, the volcanism and Fe-Cu-Mo mineralization in this area is characterized by multistage superimposed mineralization.

**Keywords: volcanic rocks, LA-ICP-MS, zircon, U-Pb, geochemistry, mineralization, northern magin of junggar**

OPEN ACCESS

***Edited by:***
*Chang-Zhi Wu,*
*Chang'an University, China*

***Reviewed by:***
*Hao Yujie,*
*Jilin University, China*
*Fuquan Yang,*
*Chinese Academy of Geological Sciences (CAGS), China*

****Correspondence:***
*Hao Wei*
*ronghaiwei@163.com*

***Specialty section:***
*This article was submitted to Economic Geology, a section of the journal Frontiers in Earth Science*

***Received:*** *22 January 2021*
***Accepted:*** *29 April 2021*
***Published:*** *21 May 2021*

***Citation:***
*Wei X, Wei H, Liao Z, Wang Z, Li D, Mao Q and Li X (2021) Geochronology and Geochemistry of Late Paleozoic Volcanic Rocks and Their Relationship With Iron and Molybdenum Deposits in Xilekuduk Area, Northern Margin of Junggar. Front. Earth Sci. 9:657083. doi: 10.3389/feart.2021.657083*

## INTRODUCTION

The Xilekuduk area in Fuyun County, Xinjiang, is located in the northern margin of the Junggar Basin, in the collision suture zone of the Siberian Plate and the Junggar Plate (Sengör et al., 1993; Windley et al., 2007). A large number of Paleozoic strata were formed during the process of plate amalgamation and accretion in the Paleozoic, with crisscross faults and strong magmatic activities forming a geological unit with complex coupling of tectonics, magmatism, and mineralization, which gave birth to an important metallogenic belt of precious gold and nonferrous metals such as iron, copper, gold, nickel, and rare metals in China (Yang et al., 2009; Yang et al., 2012; Yang et al., 2014; Li et al., 2015; Wei et al., 2019).

The porphyry Cu-Mo deposit discovered in the Xilekuduk area in 2005 is of great significance in understanding mineralization and the metallogenic series in the Junggar area. The zircon U-Pb method was applied for accurately dating the granitoids of porphyry (copper) molybdenum deposit. The diagenetic age was concentrated at 340–315 Ma, which was considered as the product of tectonic magmatic evolution of plate collision—post collision (You et al., 2016; Long et al., 2009); the Re-Os isochron age of molybdenite was 327.1 ± 2.9 Ma, and the metallogenic age was determined as early stage of Middle–Late Carboniferous (Long et al., 2011). It is considered that the source of ore-forming material and granite porphyry bear the characteristics of homologous magma (Long et al., 2014). The age data of a large number of andesitic, dacitic volcanic rocks, and pyroclastic rocks exposed in the ore district are yet to be reported. It is generally speculated that they belong to the volcanic sedimentary assemblage of the Lower Carboniferous Namingshui Formation (Long et al., 2009; Ding et al., 2011; Long et al., 2011; Long et al., 2014; You et al., 2016; Wei et al., 2019). Some new scientific issues, however, have also been raised in this study:

1) The volcanic sedimentary assemblage of intermediate acid volcanic rocks–pyroclastic rocks–carbonate rocks distributed in the ore district obviously differs from that of the marine continental interactive facies clastic sedimentary rocks of the Lower Carboniferous Namingshui Formation (the Jiangbastao Formation). Are these volcanic rocks all formed in Carboniferous as previously speculated? Are the two types of sedimentary assemblages the product of the same geological event? 2) In 2015, layered magnetite bodies that occurred at the interface between volcanic rocks and clastic rocks were successively discovered more than 100°m southwest of the porphyry copper–molybdenum deposit; their coupling relationship with volcanic rocks, however, remains unclear.

The above issues hinder our understanding of volcanism and the genesis of the deposit in this area and limit the breakthrough of mineral exploration. Therefore, on the basis of detailed field investigation, the author has carried out systematic geochronology and rock geochemistry of volcanic rocks, determined the formation age and genesis of volcanic rocks, and through mineralogical studies of two periods of magnetite, combined with regional data, discussed the volcanic magmatic events and mineralization in this area, so as to provide scientific guidance for mineral exploration in this area.

## REGIONAL GEOLOGY AND DEPOSIT CHARACTERISTICS

### Regional Geological Background

The tectonic location of the study area is located in the Gabosar Island Arc Belt of the East Junggar Orogenic Belt (You et al., 2016) (**Figure 1A**). The regional exposed strata are predominantly Paleozoic, Devonian, and Carboniferous, followed by Cenozoic tertiary and Quaternary, with local occurrence of Permian and Jurassic. Among these, the Devonian is the most widely distributed, which is a set of littoral and neritic clastic rock, volcanic lava, pyroclastic rock with carbonate rock, and terrigenous clastic rock. It is the main ore-bearing layer of iron and copper polymetallic in the area. Regional fold and fault structures are developed, mainly including the Yitieke aketas composite anticline, Sarbulak karatongke composite syncline, and Jiaposar composite anticline as well as the northwest trending Erqisi deep fault, Ulunguhe deep fault, and Kalashinger fault. Among these, the Kalashinger fault has been formed most recently as the main rock-controlling and ore-controlling fault structure in the region. The magmatic activity in the area is intense and various intrusive bodies are formed. The rock types are mainly granite. The diagenetic age is concentrated in the Early–Middle Devonian of Late Paleozoic, followed by the Early Carboniferous. The volcanic rocks mainly occur in the Devonian Tuorangekuduke, Beitashan, Yundukala, and Kashion formations, and Carboniferous Jiangbastao and Batamayineishan formations (Zhang et al., 2006; Li et al., 2015) (**Figure 1B**).

### Geological Characteristics of the Deposit

According to previous studies, the volcanic and pyroclastic rock strata exposed in the ore district are assigned to the Lower Carboniferous Nanmingshui Formation (Long et al., 2009; Ding et al., 2011; Long et al., 2011; Long et al., 2014; You et al., 2016; Wei et al., 2019). Two groups of volcanic rock–clastic rock formations were decomposed in this field investigation: one group was the combination of intermediate-basic volcanic lava–sedimentary rock, while the other was the combination of intermediate-basic volcanic lava–volcanic clastic rock–clastic sedimentary rock. The two were in a fault contact relationship (**Figure 1C**, **Figure 2**). The intermediate basic volcanic lava is mainly distributed in the northeast of the ore district, with an area of about 1.1 $km^2$ and a lithology thickness of about 520 m. Intermediate basic volcanic lava–pyroclastic rocks–clastic sedimentary rocks are mainly distributed in the northwest of the ore district, with an area of 8.9 $km^2$.

It can be divided into five volcanic rhythms with a thickness of 3018 m, showing an integrated contact relationship of volcanic eruption: 1) Overflow facies andesite-erupted andesite lithic tuff, about 57 m thick. 2) Eruptive facies stomatal and esite-falling accumulation facies volcanic sedimentary tuff, with a thickness of about 110 m. 3) Overflow facies andesite-erupted andesite lithic tuff-sedimentary facies tuffaceous sandstone, about 1540 m thick.

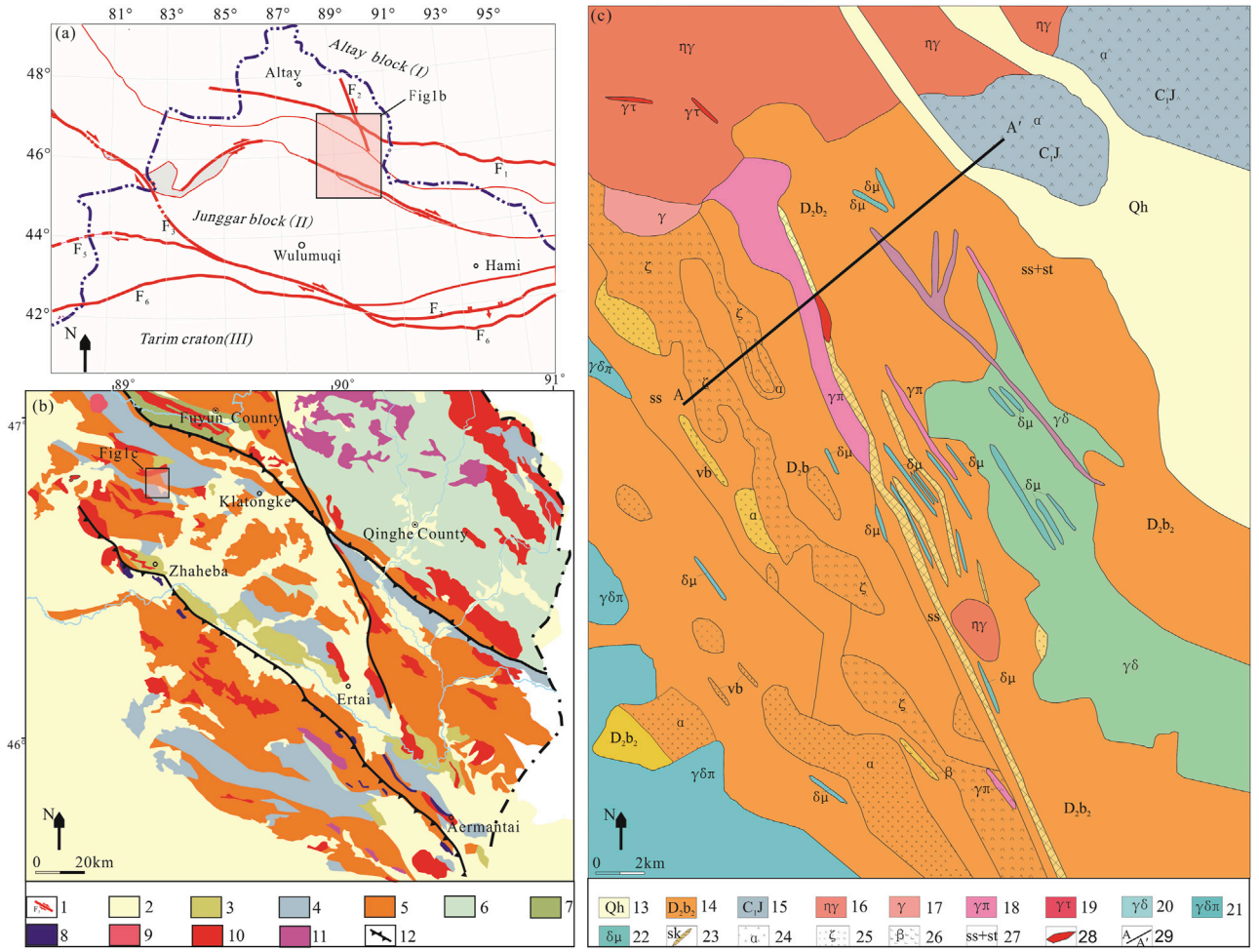


**FIGURE 1 |** (Mended according to Wei et al. (2019)). Tectonic location map **(A)**, regional geological map **(B),** and deposit geological map **(C)** in the Xilekuduk area, Fuyun County, Xinjiang. 1: regional major fault; 2: Quaternary; 3: Permian; 4: Carboniferous; 5: Devonian; 6: Silurian; 7: Precambrian; 8: ophiolite; 9: Permian granite; 10: Carboniferous granite; 11: Devonian Silurian granite; 12: suture zone; 13: Quaternary; 14: Lower Carboniferous Jiangbastao Formation; 15: Middle Devonian Beitashan formation; 16: monzogranite; 17: granite; 18: granite porphyry; 19: quartz porphyry; 20: granodiorite; 21: granite porphyry; 22: diorite porphyrite; 23: skarn belt; 24: andesite; 25: dacite; 26: basalt; 27: siltstone and sandstone; 28: iron ore body; and 29: measured section position.

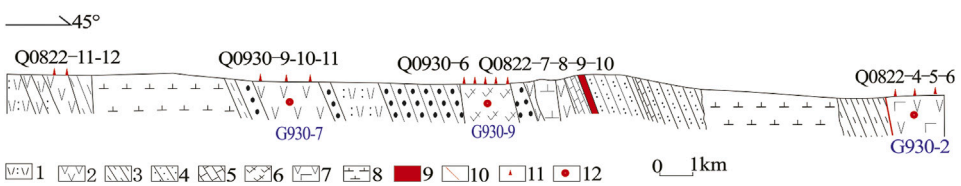


**FIGURE 2 |** Typical profile of volcanic formation distribution in Xilekuduk area, Fuyun County. 1: clastic tuff; 2: andesite; 3: sandstone; 4: siltstone; 5: skarn; 6: dacite; 7: andesite; 8: granite porphyry; 9: magnetite ore body; 10: fault; 11: geochemical sample location and number; and 12: geochronological sample location and number.

4) Overflow facies dacite-sedimentary facies tuffaceous sandstone, about 810 m thick. 5) Overflow facies andesite-sedimentary facies carbonate rock, sandstone, with a thickness of about 510 m, magnetite ore bodies are distributed in the skarnized zone of contact between pyroclastic rocks and carbonate rock. On the basis of type of rock association, the volcanic rock and clastic rock association exposed in the ore district is not completely Carboniferous.

Intrusive rocks are well developed in the ore district. Monzonitic granite, quartz porphyry, diorite porphyrite, and

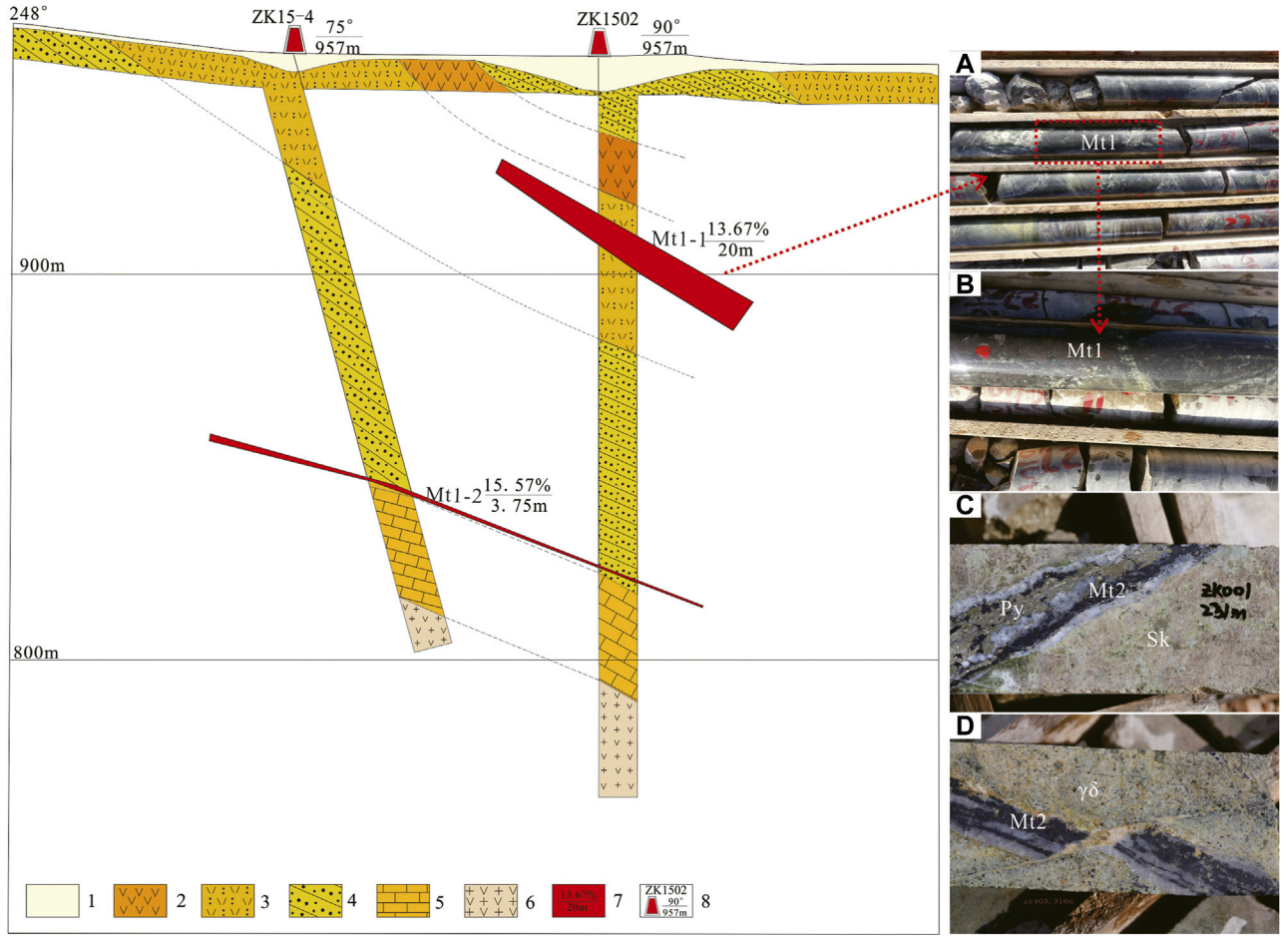


**FIGURE 3 |** Typical section of iron ore body in Xilekuduk area, Fuyun County. 1: Quaternary; 2: andesite; 3: andesitic tuff; 4: sandstone; 5: limestone; 6: diorite; 7: iron ore body; and 8: Drilling position and number Mt1: first phase magnetite; Mt2: phase II magnetite; Py: pyrite; sk: skarn; and γδ: granodiorite.

diorite occur successively from the north to the south of the ore district. Fault structures are extremely developed, comprising three main groups of NNW-NS, NW-EW, and NEE trending faults. Among them, NNW-NS fault is the most developed in the central part of the ore district, which is the main rock-controlling and ore-controlling fault in the ore district. It belongs to the secondary fault of the NW-trending regional Erqis south fault (Ablimit, 2017) (**Figure 1C**).

The Cu-Mo deposit is a concealed porphyry deposit located in the northern part of the area. It mainly occurs in the internal and external contact zone of granite porphyry, quartz diorite, and tuffaceous siltstone. The ore body is stratoid and lenticular, strikes 350°–360°, inclines to the east with dips of 25°–40°, and occurs in parallel with local pinch of outbranches. It is 100–300 m long, 90–380 m wide, and 0.84–30.37 m thick. The average grade of Mo ore body is 0.061–0.097%. The metal minerals are mainly molybdenite and pyrite, with a small amount of chalcopyrite and magnetite. The gangue minerals mainly include quartz, sericite, chlorite, and epidote. The iron ore body is located in the skarn zone at the lithologic interface between pyroclastic sedimentary rock and carbonate rock in the south of the ore district. The surface mineralization chiefly comprises a beaded or lenticular shape. The exposed ore body is 1 m thick with a Cu grade of 1.57% and TFe content of 22.6%; the magnetite ore body with a thickness of 3 m is delineated by deep drilling (**Figure 3**), and the average TFe content is 18.54%. The main mineralization types are skarn type copper (gold) ore, skarn type copper-bearing magnetite, and skarn type copper-bearing pyrrhotite magnetite.

## MATERIALS AND METHODS

### Sample Collection and Preparation

Geochronology and geochemistry samples were collected from the northeastern andesite outcrop area, the southwestern dacite outcrop area, and the southwestern andesite outcrop area of the Xilekuduk copper (molybdenum) deposit. The respective coordinates are 95°13′44″ E and 46°49′46″N, 95°13′04″E and 46°48′33″N, and 95°12′20″E and 46°48′00″N.

Selection and preparation of zircon minerals were undertaken by Langfang Regional Geological Survey Institute.

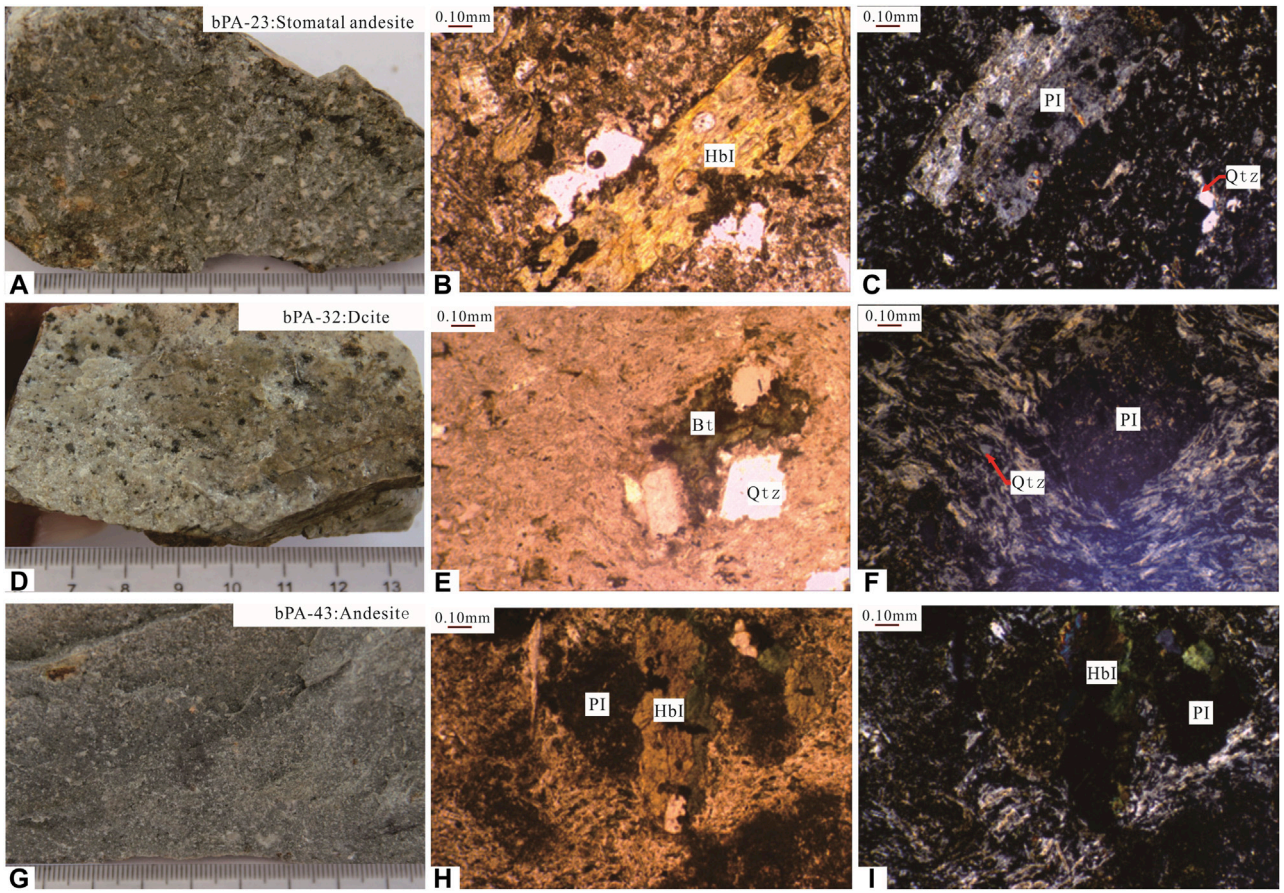


**FIGURE 4 |** Petrographic characteristics of Xilekuduk volcanic rocks. Pl: plagioclase, Hbl: hornblende, Qtz: quartz, and Bt: biotite.

## Sample Characteristics

### 1) Characteristics of Volcanic Rock Samples

According to the field observation and the measured section, the volcanic lava in the southwest of the ore district includes dacite and andesite, and the volcanic lava in the northeast is mainly stomatal andesite. The specific petrographic characteristics are as follows:

Northeast stomatal andesite: the weathered surface is gray, while the fresh surface is cyan gray, in porphyritic structure; the matrix is felsic and in fine interwoven structure and massive structure; the rock is composed of phenocrysts and the matrix (**Figure 4A**). The phenocryst minerals are plagioclase (PL) and hornblende (HBL), accounting for 15–25% of the total rock mass; the matrix is microcrystalline plagioclase, hornblende, and biotite; plagioclase is arranged in a directional manner; microcrystalline quartz is in felsic interlaced structure, accounting for about 80–85% of the total rock, and the accessory mineral is magnetite (**Figures 4B,C**).

Southwest dacite: the weathered surface is gray, while the fresh surface is grayish white, in porphyritic structure; the matrix is in felsic interlaced structure and massive structure; the rock is composed of phenocrysts and matrix (**Figure 4D**). The phenocryst minerals are plagioclase (PL), biotite, and quartz (QTZ), accounting for 8–10% of the total rock mass; the matrix is microcrystalline plagioclase, quartz, and biotite. Plagioclase is directionally arranged with quartz in felsic and fine texture, accounting for about 90–92% of the total rock mass (**Figures 4E,F**). The accessory minerals are magnetite, while the altered minerals are sericite and chlorite.

Southwest andesite: the weathered surface is grayish green while the fresh surface is greenish green (**Figure 4G**). The rocks are composed of phenocrysts and matrix. The phenocryst minerals are plagioclase (PL) and hornblende (HBL), accounting for about 10–20% of the total rock mass; the matrix is microcrystalline plagioclase, hornblende, and quartz. Plagioclase is oriented and interwoven, accounting for 85–90% of the total rock mass (**Figures 4H**,I). The accessory mineral is magnetite.

### 2) Characteristics of Magnetite Samples

There are two main occurrence types of magnetite in the study area: 1) MT1 type: stratiform magnetite ore occurring along the strata (**Figure 5A**). The surrounding rocks are mainly composed of andesitic volcanic tuff and tuffaceous siltstone (**Figures 3A,B**, **5A**). Magnetite is mainly of euhedral and subhedral texture (**Figures 5B,C**). Intergrowth granular pyrite can be seen in

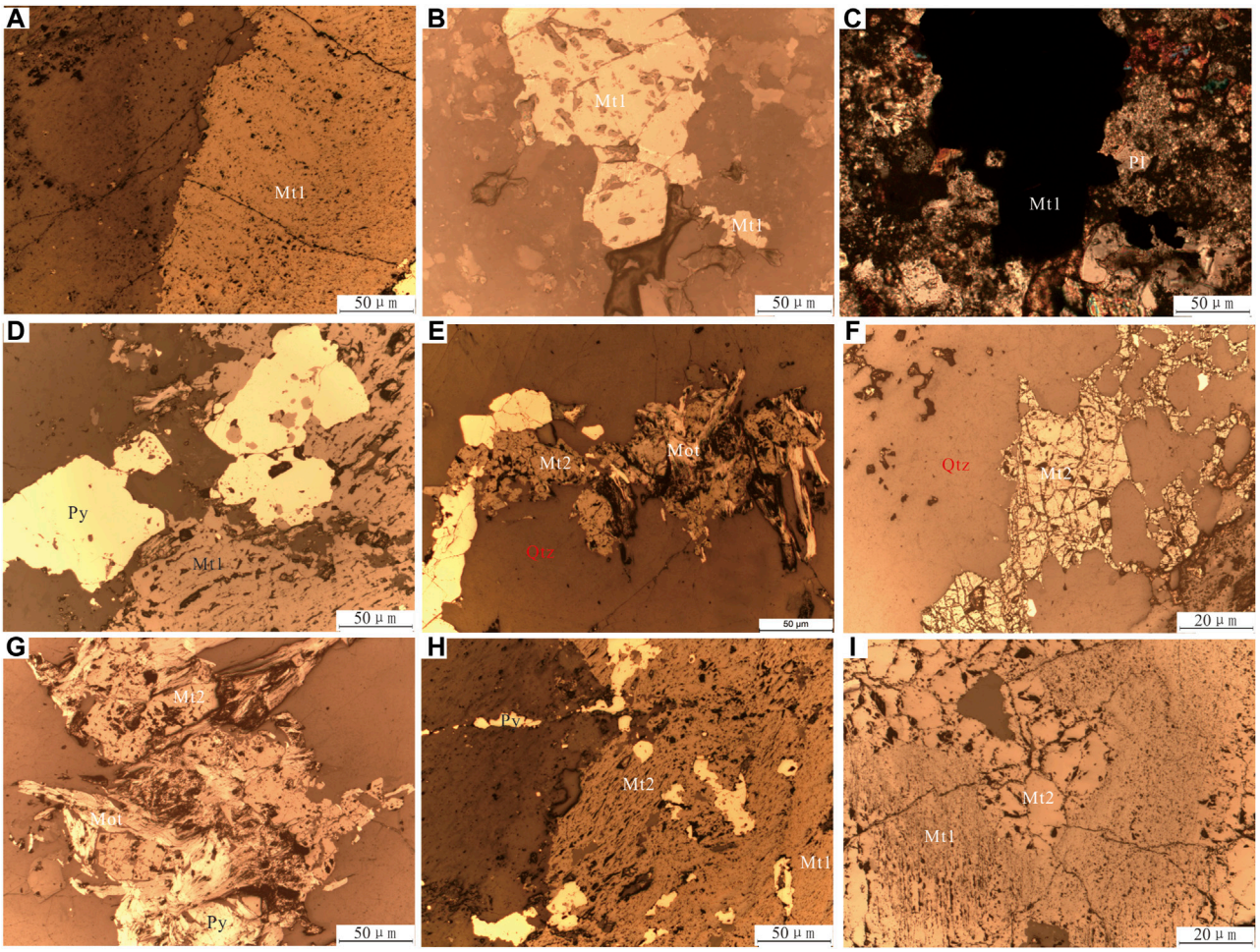


**FIGURE 5 |** Typical magnetite micrograph of Xilekuduk ore district. **(A)**: the contact boundary between early bedding stratiform magnetite ore MT1 and Devonian volcanic rocks (reflection); **(B)**: early veined euhedral–subhedral magnetite MT1 (reflection); **(C)**: early vein euhedral–subhedral magnetite MT1 (reflection +); **(D)**: intergrowth granular pyrite in MT1 magnetite; **(E)**: anhedral magnetite MT2 in late quartz vein replaced by late pyrite and molybdenite (reflection); **(F)**: anhedral magnetite MT2 in quartz veins; **(G)**: anhedral magnetite MT2 in late magnetite quartz vein is replaced by late molybdenite and pyrite (reflection); **(H)**: MT2 magnetite occurs along the contact zone between Mt1 magnetite and volcanic strata and is cut by late pyrite veins; and **(I)**: MT1 magnetite is wrapped by MT2 magnetite; Py: pyrite; Mot: molybdenite; Mt: magnetite; and Qtz: quartz.

MT1 magnetite (**Figure 5D**). 2) MT2 type: reticular vein magnetite-quartz vein (**Figures 5E–G**), are veined into the tensile fractures of skarn and diorite (**Figures 3C,D**), often replaced by late pyrite and molybdenite (**Figures 5E,G**), with poor euhedral texture and rough surface (**Figures 5F,H,I**). Some MT2 magnetite veins cut through the contact zone between MT1 magnetite and volcanic rock stratum, and are cut by late pyrite vein (**Figure 5H**). MT1 magnetite is often wrapped by MT2 magnetite, which indicates that the formation of MT2 magnetite is later than that of MT1.

## Analysis Method

### 1) Zircon U-Pb Dating

Zircon U-Pb dating was carried out in the Chinese Academy of Sciences' Guiyang Institute of Geochemistry. The test instrument was the GeoLas2005 laser ablation system produced by Agilent, company of the United States, and Elan 6100DRC ICP-MS. The laser spot diameter was 30 μm, the laser pulse was 10 Hz, the energy was 32–36 mJ, and the depth of laser ablation sample was 20–40 μm. The international standard zircon 91,500 was used as the external reference material for zircon age determination. For detailed analysis steps and data processing methods, please refer to the relevant literature (Yuan et al., 2003). The isotopic ratio and element content of zircon were calculated by Gitter (ver 4.0, Macquarie University) program and Andersen Tom (Andersen, 2002). LA-ICP-MS Common Lead Correction (ver 3.15) software was used for correction of common lead, and Isopolt (ver 3.0) software was used for age calculation and concordance diagram drawing.

### 2) Analysis of Elements

The major rare earth and trace elements were determined in the State Key Laboratory of Institute of Geology and Geophysics of the Chinese Academy of Sciences. The major elements were

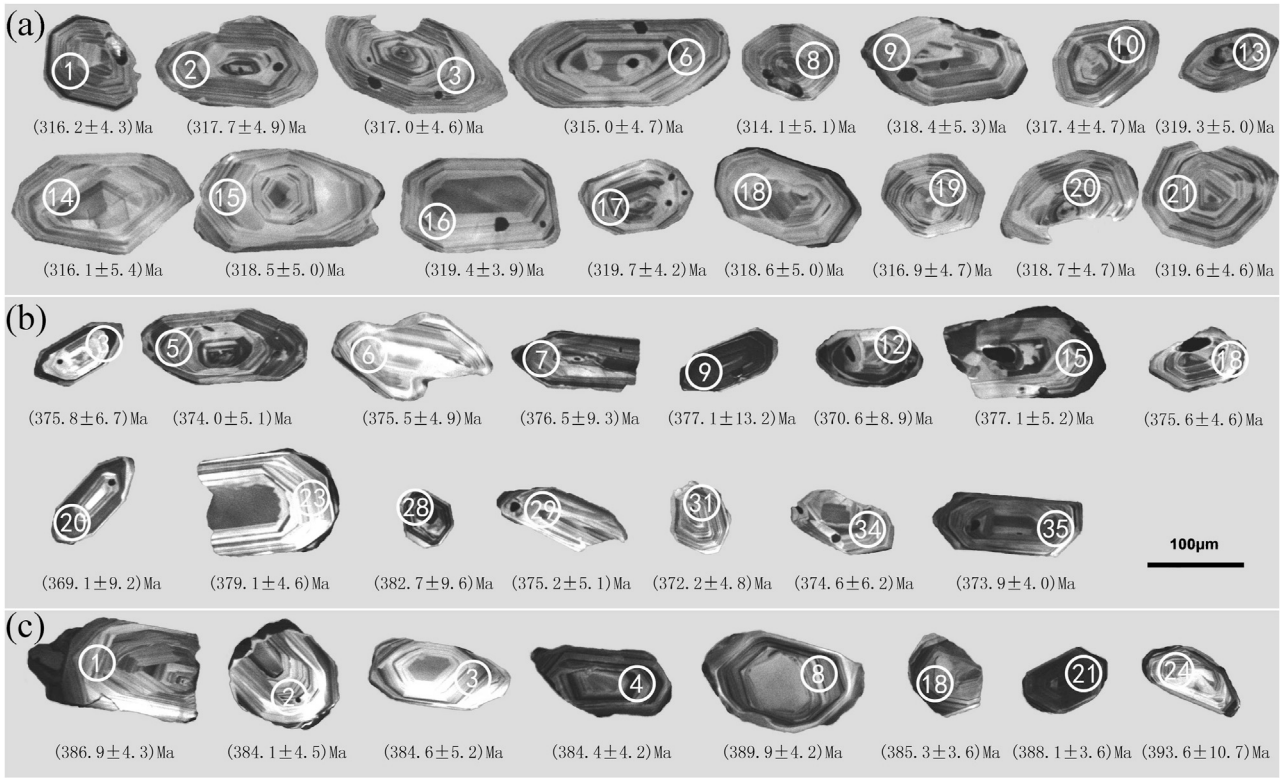


**FIGURE 6 |** Cathodoluminescence of zircon in volcanic lava. **(A)** Northeast stomatal andesite; **(B)** southwest dacite; and **(C)** southwest andesite.

determined with application of the melting XRF method (national standard GB/t14506.28–1993) on X-ray fluorescence spectrometer 3080 E. The contents of rare earth and trace elements were determined by double-focus high-resolution ICP-MS produced by Finnigan MAT.

# RESULTS

## LA-ICP-MS Geochronology of Zircon

The zircons in the stomatal andesite of the northeast area were mostly subhedral long columnar, with clear crystal edges and planes in the grains; grain lengths varied from 70 to 220 μm, while grain widths varied from 30 to 80 μm. The ratios of the grain length and width were within 1:1 to 1:10. The weight abundances of uranium (w (U)) in zircons were (222.56–360.80) $\times 10^{-6}$ and the weight abundances of thorium (w (Th)) were (74.26–381.45) $\times 10^{-6}$, while the ratio of Th/U was 0.55–0.92, further above 0.1. The zircons in dacite and andesite in the southwest area were mostly hypidiomorphic short columnar to long columnar with clear crystal edges and planes in the grains. The grain lengths varied from 50 to 120 $\mu$ m, the grain widths ranged from 30 to 80 $\mu$m, and the ratios of the grain length and width were within 1:1 to 1:8. The w (U) in zircons were (212.19–699.10)×10$_{-6}$ and (329.60–4273.32)$\times 10^{-6}$, respectively, w (th) were (138.62–969.58)$\times 10^{-6}$ and (161.84–4582.81)×10–6, respectively, Th/U ratio was 0.42–0.92 (except G930-7–2 = 1.22, G930-7–9 = 1.10), and 0.23–0.63 (except G930-9–29 = 1.07). Combined with the cathodoluminescence image (CL) (**Figure 6**), these zircons have a typical oscillatory rhythmic zoning structure and belong to magmatic origin (Courfu et al., 2003).

The zircon U-Pb isotopic analysis data of volcanic rocks (**Table 1**) show that they are more consistent within the error range in the values of $^{207}Pb/^{235}U$ and $^{206}Pb/^{238}U$, and the data fall on and near the concordant curve, the $^{206}Pb/^{238}U$ age of andesite in the northeast area was between (311 ± 4.6) to (319 ± 4.6) Ma, and its weighted average was (317.9 ± 2.9) Ma, with the weighted mean variance (MSWD) being 0.13, which can categorize the corresponding diagenetic age to the Lower Carboniferous (**Figure 7A**). The $^{206}Pb/^{238}U$ ages of the dacite in the southwestern area ranged from 373 ± 5.1 Ma to 393 ± 10.7 Ma, and its weighted average was 375.2 ± 2.9 Ma (MSWD = 0.20) (**Figure 7B**). The $^{206}Pb/^{238}U$ ages of the southern porous andesite were between 369 ± 9.2 Ma to 382 ± 9.6 Ma, and its weighted average was 386.5 ± 3.0 Ma (MSWD = 0.30), with the diagenetic age corresponding to the Middle and Late Devonian (**Figure 7C**).

## Petrogeochemistry

### 1) Major Element Geochemistry

The results of major elements of volcanic rocks are shown in **Table 2**. The $SiO_2$ content of Carboniferous stomatal andesite was between 55.01 and 55.80%, and the $SiO_2$ content was relatively low. The $Al_2O_3$ content was between 17.08 and 17.48%, the CaO content was between 5.86 and 6.11%, and the content of MgO was

**TABLE 1 |** Zircon isotopic analysis results of volcanic rocks in the Xilekuduk area.

| Point Number | Lithology | Element content ($\times 10^{-6}$) | | | Th/U | Isotope ratio | | | | | | Age (Ma) | | | | | |
|---|---|---|---|---|---|---|---|---|---|---|---|---|---|---|---|---|---|
| | | Pb | Th | U | | $^{207}Pb/^{206}Pb$ | 1σ | $^{207}Pb/^{235}u$ | 1σ | $^{207}Pb/^{238}u$ | 1σ | $^{207}Pb/^{206}Pb$ | 1σ | $^{207}Pb/^{235}u$ | 1σ | $^{206}Pb/^{238}u$ | 1σ |
| G930-2–1 | Northeast stomatal andesite | 32.74 | 223.89 | 335.41 | 0.67 | 0.06126 | 0.00445 | 0.39376 | 0.01994 | 0.05027 | 0.00070 | 650.0 | 157.4 | 337.1 | 14.5 | 316.2 | 4.3 |
| G930-2–2 | (Carboniferous) | 30.14 | 142.55 | 222.56 | 0.64 | 0.06257 | 0.00513 | 0.41283 | 0.03280 | 0.05052 | 0.00080 | 694.5 | 174.8 | 350.9 | 23.6 | 317.7 | 4.9 |
| G930-2–3 | | 28.79 | 155.32 | 264.16 | 0.59 | 0.06853 | 0.00455 | 0.45079 | 0.02548 | 0.05041 | 0.00075 | 884.9 | 137.0 | 377.8 | 17.8 | 317.0 | 4.6 |
| G930-2–6 | | 28.84 | 201.93 | 301.36 | 0.67 | 0.06270 | 0.00467 | 0.40463 | 0.02733 | 0.05008 | 0.00076 | 698.2 | 159.2 | 345.0 | 19.8 | 315.0 | 4.7 |
| G930-2–8 | | 34.01 | 310.65 | 381.20 | 0.81 | 0.05655 | 0.00343 | 0.36707 | 0.02027 | 0.04993 | 0.00082 | 472.3 | 133.3 | 317.5 | 15.1 | 314.1 | 5.1 |
| G930-2–9 | | 22.63 | 178.65 | 260.67 | 0.69 | 0.06437 | 0.00766 | 0.40826 | 0.03000 | 0.05064 | 0.00087 | 753.7 | 253.7 | 347.6 | 21.6 | 318.4 | 5.3 |
| G930-2–10 | | 28.49 | 196.88 | 318.45 | 0.62 | 0.04796 | 0.00315 | 0.32328 | 0.01850 | 0.05046 | 0.00077 | 98.2 | 157.4 | 284.4 | 14.2 | 317.4 | 4.7 |
| G930-2–13 | | 56.66 | 481.80 | 522.77 | 0.92 | 0.05973 | 0.00308 | 0.40840 | 0.01972 | 0.05079 | 0.00081 | 594.5 | 112.9 | 347.7 | 14.2 | 319.3 | 5.0 |
| G930-2–14 | | 33.95 | 241.93 | 315.46 | 0.77 | 0.07316 | 0.00552 | 0.45003 | 0.02631 | 0.05026 | 0.00088 | 1018.2 | 153.7 | 377.3 | 18.4 | 316.1 | 5.4 |
| G930-2–15 | | 21.21 | 128.09 | 231.39 | 0.55 | 0.05739 | 0.00491 | 0.36533 | 0.02392 | 0.05065 | 0.00082 | 505.6 | 188.9 | 316.2 | 17.8 | 318.5 | 5.0 |
| G930-2–16 | | 51.62 | 400.17 | 494.51 | 0.81 | 0.04816 | 0.00263 | 0.33496 | 0.01628 | 0.05079 | 0.00063 | 105.6 | 125.9 | 293.3 | 12.4 | 319.4 | 3.9 |
| G930-2–17 | | 50.02 | 381.45 | 480.58 | 0.79 | 0.05920 | 0.00317 | 0.41147 | 0.01987 | 0.05084 | 0.00068 | 576.0 | 116.7 | 349.9 | 14.3 | 319.7 | 4.2 |
| G930-2–18 | | 25.54 | 183.85 | 288.49 | 0.64 | 0.05914 | 0.00385 | 0.38626 | 0.02165 | 0.05066 | 0.00082 | 572.3 | 137.9 | 331.6 | 15.9 | 318.6 | 5.0 |
| G930-2–19 | | 34.90 | 269.07 | 348.05 | 0.77 | 0.07653 | 0.00563 | 0.48958 | 0.03078 | 0.05039 | 0.00077 | 1109.3 | 148.1 | 404.6 | 21.0 | 316.9 | 4.7 |
| G930-2–20 | | 32.40 | 224.18 | 360.80 | 0.62 | 0.05454 | 0.00339 | 0.37580 | 0.02003 | 0.05069 | 0.00077 | 394.5 | 136.1 | 323.9 | 14.8 | 318.7 | 4.7 |
| G930-2–21 | | 31.78 | 249.23 | 344.24 | 0.72 | 0.06441 | 0.00393 | 0.44703 | 0.02616 | 0.05082 | 0.00075 | 755.3 | 129.6 | 375.2 | 18.4 | 319.6 | 4.6 |
| G930-7–3 | Southwest dacite (Devonian) | 38.37 | 235.64 | 370.43 | 0.64 | 0.06857 | 0.00463 | 0.54918 | 0.03570 | 0.06003 | 0.00111 | 887.0 | 140.7 | 444.5 | 23.4 | 375.8 | 6.8 |
| G930-7–5 | | 27.99 | 138.62 | 332.90 | 0.42 | 0.06251 | 0.00372 | 0.49359 | 0.02470 | 0.05973 | 0.00084 | 700.0 | 123.1 | 407.4 | 16.8 | 374.0 | 5.1 |
| G930-7–6 | | 44.07 | 269.86 | 380.11 | 0.71 | 0.06262 | 0.00326 | 0.51063 | 0.02258 | 0.05998 | 0.00080 | 694.5 | 305.5 | 418.9 | 15.2 | 375.5 | 4.9 |
| G930-7–7 | | 28.63 | 153.40 | 309.76 | 0.50 | 0.06471 | 0.00662 | 0.51567 | 0.06439 | 0.06015 | 0.00152 | 764.8 | 218.5 | 422.3 | 43.1 | 376.5 | 9.3 |
| G930-7–9 | | 100.00 | 810.27 | 666.26 | 1.22 | 0.06172 | 0.00597 | 0.52639 | 0.06318 | 0.06024 | 0.00218 | 664.8 | 208.2 | 429.4 | 42.0 | 377.1 | 13.2 |
| G930-7–12 | | 68.56 | 460.83 | 498.81 | 0.92 | 0.07179 | 0.00524 | 0.61035 | 0.06537 | 0.05917 | 0.00146 | 988.9 | 144.3 | 483.8 | 41.2 | 370.6 | 8.9 |
| G930-7–15 | | 58.33 | 321.77 | 589.25 | 0.55 | 0.05576 | 0.00251 | 0.48686 | 0.02026 | 0.06024 | 0.00086 | 442.6 | 100.0 | 402.8 | 13.8 | 377.1 | 5.2 |
| G930-7–18 | | 70.42 | 413.04 | 498.38 | 0.83 | 0.06703 | 0.00287 | 0.55371 | 0.02219 | 0.06000 | 0.00076 | 838.9 | 89.7 | 447.4 | 14.5 | 375.6 | 4.6 |
| G930-7–20 | | 71.85 | 508.37 | 699.10 | 0.73 | 0.05919 | 0.00330 | 0.49720 | 0.04633 | 0.05893 | 0.00151 | 572.3 | 122.2 | 409.8 | 31.4 | 369.1 | 9.2 |
| G930-7–23 | | 49.85 | 280.32 | 469.37 | 0.60 | 0.05771 | 0.00268 | 0.48136 | 0.02161 | 0.06057 | 0.00075 | 520.4 | 101.8 | 399.0 | 14.8 | 379.1 | 4.6 |
| G930-7–28 | | 133.48 | 969.58 | 883.65 | 1.10 | 0.06981 | 0.00331 | 0.57612 | 0.03283 | 0.06117 | 0.00159 | 924.1 | 97.4 | 462.0 | 21.2 | 382.7 | 9.6 |
| G930-7–29 | | 56.38 | 345.83 | 502.50 | 0.69 | 0.05325 | 0.00271 | 0.46401 | 0.02120 | 0.05993 | 0.00083 | 338.9 | 114.8 | 387.0 | 14.7 | 375.2 | 5.1 |
| G930-7–31 | | 62.23 | 369.78 | 527.78 | 0.70 | 0.05900 | 0.00276 | 0.47669 | 0.02070 | 0.05944 | 0.00079 | 568.6 | 101.8 | 395.8 | 14.2 | 372.2 | 4.8 |
| G930-7–34 | | 16.65 | 74.26 | 212.19 | 0.35 | 0.05803 | 0.00368 | 0.45874 | 0.02595 | 0.05984 | 0.00102 | 531.5 | 138.9 | 383.4 | 18.1 | 374.6 | 6.2 |
| G930-7–35 | | 84.87 | 449.63 | 883.47 | 0.51 | 0.05904 | 0.00272 | 0.50439 | 0.02495 | 0.05972 | 0.00066 | 568.6 | 100.0 | 414.7 | 16.8 | 373.9 | 4.0 |
| G930-9–1 | Southwest andesite | 43.48 | 211.51 | 594.09 | 0.36 | 0.05516 | 0.00231 | 0.46955 | 0.01867 | 0.06185 | 0.00070 | 416.7 | 94.4 | 390.9 | 12.9 | 386.9 | 4.3 |
| G930-9–2 | (Devonian) | 56.25 | 313.88 | 622.97 | 0.50 | 0.05805 | 0.00250 | 0.48572 | 0.01961 | 0.06139 | 0.00073 | 531.5 | 99.1 | 402.0 | 13.4 | 384.1 | 4.5 |
| G930-9–3 | | 36.87 | 205.05 | 329.60 | 0.62 | 0.05396 | 0.00267 | 0.45539 | 0.02094 | 0.06148 | 0.00086 | 368.6 | 111.1 | 381.0 | 14.6 | 384.6 | 5.2 |
| G930-9–4 | | 155.86 | 909.27 | 1439.80 | 0.63 | 0.05363 | 0.00197 | 0.47689 | 0.01630 | 0.06144 | 0.00069 | 353.8 | 50.9 | 395.9 | 11.2 | 384.4 | 4.2 |
| G930-9–8 | | 40.05 | 161.84 | 696.38 | 0.23 | 0.05830 | 0.00256 | 0.49823 | 0.02077 | 0.06235 | 0.00069 | 542.6 | 96.3 | 410.5 | 14.1 | 389.9 | 4.2 |
| G930-9–18 | | 124.95 | 534.33 | 1281.81 | 0.42 | 0.06696 | 0.00228 | 0.57468 | 0.01945 | 0.06160 | 0.00059 | 836.7 | 70.4 | 461.0 | 12.5 | 385.3 | 3.6 |
| G930-9–21 | | 649.40 | 4582.81 | 4273.32 | 1.07 | 0.05502 | 0.00157 | 0.47922 | 0.01320 | 0.06205 | 0.00060 | 413.0 | 64.8 | 397.5 | 9.1 | 388.1 | 3.6 |
| G930-9–24 | | 86.32 | 339.38 | 1051.04 | 0.32 | 0.05886 | 0.00253 | 0.49288 | 0.02914 | 0.06296 | 0.00177 | 561.1 | 94.4 | 406.9 | 19.8 | 393.6 | 10.7 |

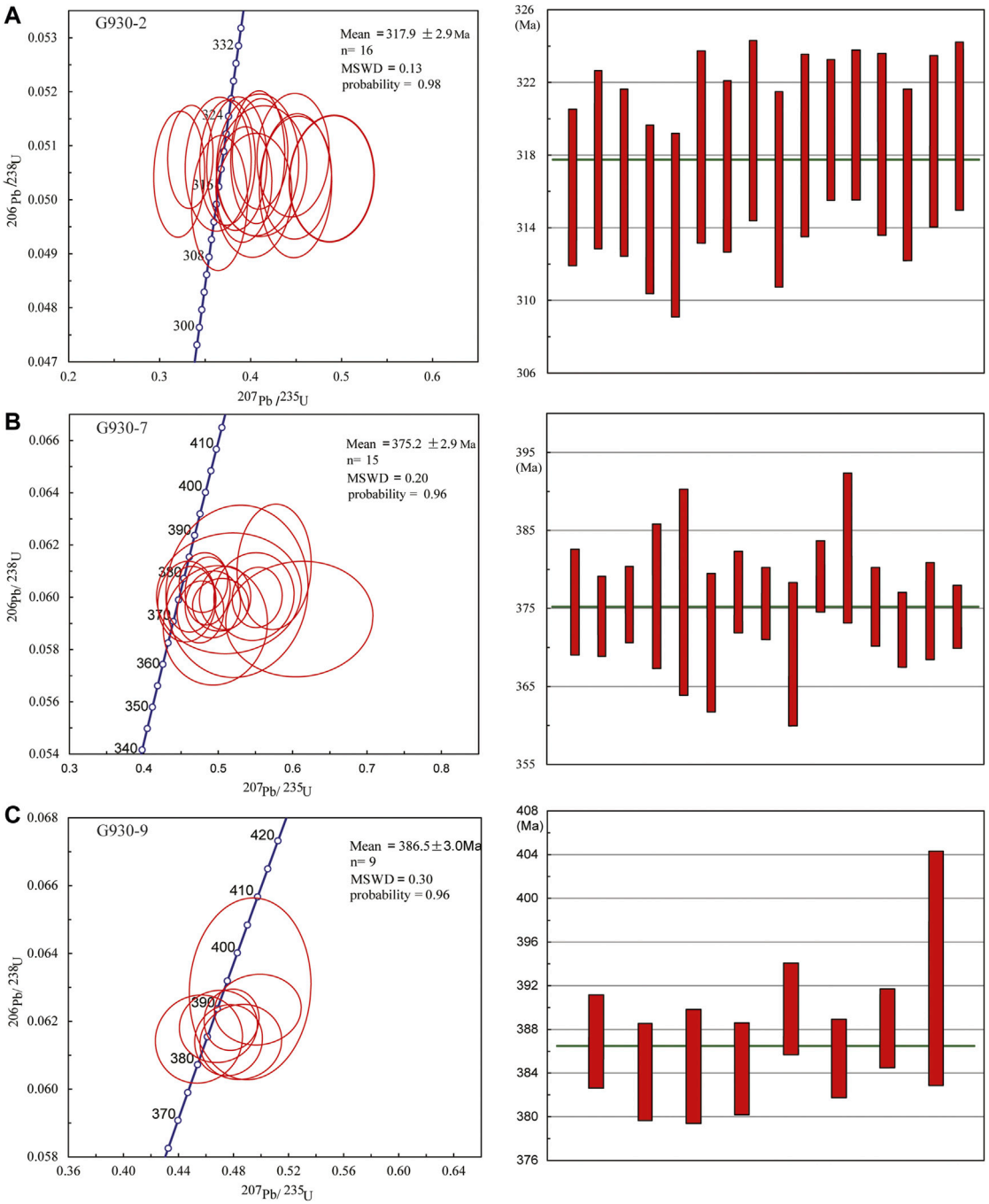


**FIGURE 7 |** Concordant age diagram and weighted mean age of LA-ICP-MS zircon $^{207}Pb/^{235}U$-$^{206}Pb/^{238}U$ of volcanic lava in Xilekuduk area. **(A)** Northeast stomatal andesite; **(B)** southwest dacite; and **(C)** southwest andesite.

between 4.36 and 4.40%. The $Fe_2O_3$ content ranged from 3.77 to 3.82%; $TiO_2$ varied between 0.94 and 0.97%, and the content of $TiO_2$ was relatively high. The total alkali content ranged from 5.77 to 6.30% and sodium rich ($Na_2O/K_2O$ = 3.05–3.60); the Mg number is 33.45–36.01, the consolidation index (SI), the feldspar index (FL), and the iron magnesium index (MF) were relatively low, as shown in **Table 3**.

The $SiO_2$ content of Devonian dacite ranged from 62.25 to 63.08%; the $Al_2O_3$ content 16.85–17.58%; the CaO content 2.57–3.64%; the MgO content 1.18–1.51%; the $Fe_2O_3$ content 0.84–1.04%; and the TiO2 content 0.34–0.35%. The total alkali content was between 7.45 and 9.00%, and it was rich in sodium ($Na_2O/K_2O$ = 1.33–1.88). The $SiO_2$ content of Devonian andesite ranged from 61.89 to 62.71%; the $Al_2O_3$ content

**TABLE 2 |** Major element analysis data of volcanic rocks in the Xilekuduk area (wt%).

| Sample number | Lithology | $SiO_2$ | $TiO_2$ | $Al_2O_3$ | $Fe_2O_3$ | MgO | MnO | CaO | $Na_2O$ | $K_2O$ | $P_2O_5$ | FeO | LOI[1] | Total |
|---|---|---|---|---|---|---|---|---|---|---|---|---|---|---|
| Q0822–4 | Northeast stomatal andesite (Carboniferous) | 55.80 | 0.94 | 17.08 | 3.79 | 4.36 | 0.15 | 5.95 | 4.63 | 1.52 | 0.28 | 3.62 | 1.71 | 99.83 |
| Q0822–5 | | 55.76 | 0.97 | 17.24 | 3.77 | 4.40 | 0.17 | 6.11 | 4.50 | 1.27 | 0.28 | 3.72 | 1.66 | 99.85 |
| Q0822–6 | | 55.01 | 0.96 | 17.48 | 3.82 | 4.37 | 0.15 | 5.86 | 4.93 | 1.37 | 0.28 | 3.72 | 1.89 | 99.83 |
| Q930–6 | Southwest dacite (Devonian) | 62.78 | 0.34 | 17.53 | 0.90 | 1.18 | 0.12 | 3.10 | 4.82 | 2.63 | 0.29 | 3.71 | 2.23 | 99.63 |
| Q0822–7 | | 63.08 | 0.35 | 16.85 | 1.04 | 1.44 | 0.11 | 2.57 | 5.14 | 3.86 | 0.23 | 3.14 | 2.01 | 99.82 |
| Q0822–8 | | 63.08 | 0.35 | 17.34 | 0.76 | 1.30 | 0.12 | 3.64 | 5.07 | 2.68 | 0.22 | 3.24 | 2.02 | 99.82 |
| Q0822–9 | | 62.85 | 0.35 | 17.58 | 0.96 | 1.32 | 0.11 | 2.93 | 5.24 | 3.30 | 0.23 | 2.95 | 2.00 | 99.81 |
| Q0822–10 | | 62.25 | 0.34 | 17.03 | 0.84 | 1.51 | 0.13 | 3.14 | 5.06 | 3.57 | 0.22 | 3.54 | 2.18 | 99.82 |
| Q930–9 | Southwest andesite (Devonian) | 62.71 | 0.42 | 16.62 | 1.64 | 1.72 | 0.15 | 2.94 | 5.24 | 0.99 | 0.38 | 3.45 | 3.26 | 99.52 |
| Q930–10 | | 61.89 | 0.43 | 16.85 | 1.18 | 1.72 | 0.17 | 3.56 | 5.11 | 0.98 | 0.39 | 3.84 | 3.38 | 99.50 |
| Q930–11 | | 60.83 | 0.42 | 17.89 | 1.76 | 1.75 | 0.15 | 2.74 | 4.63 | 1.15 | 0.36 | 3.61 | 3.96 | 99.25 |
| Q0822–11 | | 62.16 | 0.47 | 17.82 | 1.54 | 1.76 | 0.14 | 2.76 | 5.59 | 1.31 | 0.36 | 3.29 | 2.67 | 99.87 |
| Q0822–12 | | 62.48 | 0.46 | 17.83 | 1.56 | 1.87 | 0.14 | 2.66 | 5.28 | 1.40 | 0.29 | 3.33 | 2.56 | 99.87 |

[1]*LOI: Loss on ignition.*

**TABLE 3 |** Geochemical parameters of volcanic rocks.

| Sample number | Lithology | Mg#[1] | Alkali value | AR[2] | A/CNK | A/NK | SI[3] | FL[4] | MF[5] | σ[6] |
|---|---|---|---|---|---|---|---|---|---|---|
| Q0822–4 | Northeast stomatal andesite (Carboniferous) | 35.98 | 1.73 | 0.32 | 2.78 | 19.51 | 50.81 | 73.09 | 2.95 | 2.95 |
| Q0822–5 | | 33.45 | 1.66 | 0.34 | 2.99 | 19.82 | 48.58 | 73.22 | 2.61 | 2.61 |
| Q0822–6 | | 36.01 | 1.74 | 0.33 | 2.78 | 19.21 | 51.78 | 73.44 | 3.30 | 3.30 |
| Q930–6 | Southwest dacite (Devonian) | 42.50 | 2.13 | 0.29 | 2.35 | 8.64 | 70.62 | 80.97 | 2.81 | 2.81 |
| Q0822–7 | | 53.45 | 2.73 | 0.22 | 1.87 | 9.63 | 77.83 | 75.86 | 4.04 | 4.04 |
| Q0822–8 | | 44.69 | 2.17 | 0.27 | 2.24 | 9.68 | 68.04 | 77.05 | 2.99 | 2.99 |
| Q0822–9 | | 48.56 | 2.43 | 0.25 | 2.06 | 9.37 | 74.47 | 76.23 | 3.67 | 3.67 |
| Q0822–10 | | 50.64 | 2.49 | 0.23 | 1.97 | 10.12 | 73.30 | 76.00 | 3.87 | 3.87 |
| Q930–9 | Southwest andesite (Devonian) | 37.48 | 1.93 | 0.42 | 2.67 | 12.81 | 67.94 | 76.09 | 1.97 | 1.97 |
| Q930–10 | | 36.14 | 1.85 | 0.41 | 2.77 | 12.97 | 63.11 | 76.00 | 1.96 | 1.96 |
| Q930–11 | | 32.31 | 1.78 | 0.46 | 3.10 | 13.16 | 67.84 | 76.73 | 1.87 | 1.87 |
| Q0822–11 | | 38.74 | 2.01 | 0.40 | 2.58 | 12.73 | 71.43 | 74.64 | 2.49 | 2.49 |
| Q0822–12 | | 37.51 | 1.97 | 0.40 | 2.67 | 13.51 | 71.52 | 73.82 | 2.29 | 2.29 |

[1]$Mg^{\#} = 100\times Molar Mg^{2+}/(Mg^{2+}+Fe^{2+})$
[2]*Alkalinity rate*
[3]*Consolidation index*
[4]*Feldspar quartz index*
[5]*Iron-magnesium index*
[6]*Rittman index.*

16.62–17.89%; the CaO content 2.66–3.56%; the MgO content 1.18–1.51%; the $Fe_2O_3$ content 0.84–1.04%; and the $TiO_2$ content 0.34–0.35%. The total alkali content is between 5.78 and 6.68%, and it is sodium-rich and potassium-poor ($Na_2O/K_2O$ = 3.77–5.29), Mg number is 42.50–53.45 and 32.31–38.74, respectively. The consolidation index (SI), the felsic index (FL), and the iron-magnesium index (MF) increase compared with the non-amygdaloid ones, indicating a high degree of magmatic crystallization differentiation (**Table 3**).

On the TAS ($SiO_2/(K_2O+ Na_2O)$) diagram of volcanic rocks (**Figure 8A**), the samples of Carboniferous mainly fall on basaltic trachyandesite, while the Devonian samples fall on the trachydacite and trachyte-andesite. On the $SiO_2/K_2O$ diagram (Harris et al., 1986) (**Figure 8B**), the samples fall into calc-alkaline basaltic andesite, andesite, and high-potassium series (andesite) dacite, respectively.

## 2) Geochemistry of Rare Earth and Trace Elements

The results of rare earth elements (REEs) and trace elements are shown in **Table 4**. The weight abundance (w ($\sum$ REE)) of the Carboniferous stomatal andesite samples and their values of europium anomaly (δ Eu) and the values of $(La)_N/(Yb)_N$ are $(95.54–116.07)\times10^{-6}$, 1.14–1.16, and 5.93–8.35, respectively. The diagram of chondrite-normalized REE distribution curve (**Figure 9A**) shows that the rocks are slightly enriched in LREE and have no obvious Eu anomaly, implying that there was no obvious fractional crystallization of

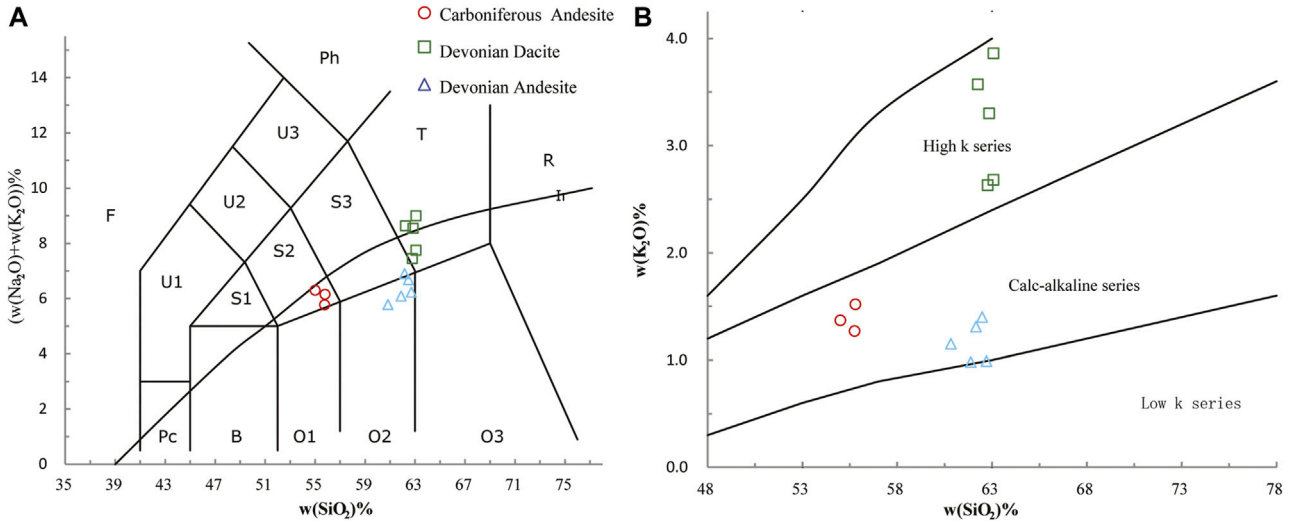


**FIGURE 8 |** TAS classification of volcanic rocks and diagram of silica alkali distribution (Irvine and Baragar, 1971). PC: picrite basalt; B: basalt; O1: basaltic andesite; O2: andesite; O3: dacite; R: rhyolite; S1: trachyte basalt; S2: basaltic trachyandesite; S3: trachyandesite; T: trachyte trachydacite; F: accessory feldspar; U1: alkali basaltic; U2: phonotic alkali basaltic rock; U3: shoshonitic phonolite; Ph: phonolite; and Ir: Irvine boundary, alkaline above and subalkaline below.

plagioclase during the magmatic evolution. The primitive mantle standard diagram of incompatible elements (**Figure 9C**) shows that large ion lithophile elements (LILEs) are relatively enriched and the high-field strength elements (HFSEs) are relatively depleted.

The w (∑ REE) of Devonian dacite samples varies slightly 108.16–130.96 × $10^{-6}$, *d* Eu is 0.97–1.16, and w $(La)_N/(Yb)_N$ is 5.67–7.65. The w (∑ REE) of Devonian andesite is 108.26–130.02 × $10^{-6}$, *d* Eu is 0.84–1.09, and w $(La)_N/(Yb)_N$ is 5.12–7.73. The normalized REE distribution curve of chondrite (**Figure 9B**) shows right-leaning LREE enrichment type, and there is no Eu anomaly in the Devonian dacites and andesites. On the primitive mantle standard diagram of incompatible elements (**Figure 9D**), the LILEs are relatively enriched and the LILEs are relatively depleted.

# DISCUSSION

## Diagenetic Age and Tectonic Environment

As predecessors have speculated, andesitic, dacitic volcanic rocks and pyroclastic rocks exposed in the ore district belong to the volcanic sedimentary assemblage of the Lower Carboniferous Namingshui Formation (Long et al., 2009; Ding et al., 2011; Long et al., 2011; Long et al., 2014; You et al., 2016; Wei et al., 2019). However, in this study, LA-ICP-MS zircon U-Pb data show that the diagenetic age of dacite is 375.2 ± 2.9 Ma and that of andesite is 386.5 ± 3.0 Ma, indicating that the volcanic rock was formed in the Middle Devonian and the basaltic andesite is 317.9 ± 2.9 Ma, corresponding to the early Late Carboniferous. According to the 1:250000 and 1:50000 regional geological survey data and previous studies, there is a set of Middle Devonian Beitashan Formation mainly composed of shallow and coastal volcanic rocks, pyroclastic rocks, and carbonate rocks, and a set of Late Carboniferous Jiangbastao Formation mainly composed of marine and continental facies clastic rocks (Zhang et al., 2005; Zhang et al., 2008). Based on this, the strata in this area can be divided into two sets: the dacite-pyroclastic rocks in the southeast belong to the Beitashan Formation of Middle Devonian, and the clastic sedimentary rocks with stomatal andesite volcanic rocks in the northwest belong to the Lower Carboniferous Jiangbastao Formation.

The Devonian volcanic rock assemblage consists of andesite and dacite. The content of $TiO_2$ varies from 0.34 to 0.35% and from 0.42 to 0.47%, which belongs to high-K calc-alkaline series. The REE standard distribution model belongs to the LREE enrichment type and the large ion lithophile elements Rb, Ba, and K are strongly enriched, and the high-field strength elements (HFSEs) Nb, Ta, and Ti are relatively depleted. The Zr/Nb ratio is 15.38–23.90, which is close to the Zr/Nb ratio range of MORB (10–60, Davisin, 1996), and the Nb/Ta ratio is 9.41–12.14, which are lower than those of the original mantle (–17), indicating that Nb and Ta are separated by subducting fluid metasomatism of the original mantle (Othman et al., 1989). The geochemical characteristics of the volcanic rocks are similar to those of the Beitashan Formation in the region and are typical island arc volcanic rocks (Deng et al., 2009). The Carboniferous volcanic rocks are mainly stomatal andesite the REE standard distribution pattern belongs to LREE enrichment type. There is no obvious negative Ce anomaly, showing obvious continental volcanic characteristics (Zhang et al., 2006). The large ion lithophile elements Th, Rb, Ba, and K are strongly enriched, and the HFSEs Nb, Ta, and Ti are relatively depleted, which are similar to island arc basalt. However, the variation of $TiO_2$ content is 0.94–0.97%, and that of V content is 178–183×$10^{-6}$, which is higher than that of island arc basalt. The metamorphic basicity of

**TABLE 4 |** Analysis data of rare earth elements and trace elements in the Xilekuduk area ($10^{-6}$).

| Lithology | Q0822–4 | Q0822–5 | Q0822–6 | Q930–6 | Q0822–7 | Q0822–8 | Q0822–9 | Q0822–10 | Q930–9 | Q930–10 | Q930–11 | Q0822–11 | Q0822–12 |
|---|---|---|---|---|---|---|---|---|---|---|---|---|---|
| | Carboniferous stomatal andesite | | | Devonian dacite | | | | | Devonian andesite | | | | |
| La | 28.36 | 22.20 | 18.60 | 21.00 | 23.57 | 26.33 | 22.87 | 24.48 | 21.40 | 22.30 | 23.80 | 26.47 | 36.62 |
| Ce | 40.46 | 41.71 | 34.94 | 43.40 | 45.91 | 50.26 | 43.81 | 46.52 | 41.90 | 56.20 | 52.30 | 47.09 | 44.00 |
| Pr | 5.07 | 5.49 | 4.55 | 5.40 | 5.71 | 6.32 | 5.46 | 5.90 | 5.23 | 5.50 | 5.66 | 6.16 | 6.18 |
| Nd | 22.27 | 24.03 | 19.60 | 21.70 | 23.60 | 25.90 | 22.58 | 24.20 | 21.60 | 22.20 | 22.20 | 25.65 | 25.76 |
| Sm | 4.62 | 4.99 | 4.01 | 3.92 | 4.30 | 4.65 | 4.08 | 4.41 | 4.36 | 4.42 | 4.85 | 5.03 | 5.01 |
| Eu | 1.54 | 1.66 | 1.35 | 1.14 | 1.45 | 1.57 | 1.40 | 1.49 | 1.13 | 1.16 | 1.20 | 1.62 | 1.62 |
| Gd | 3.59 | 3.99 | 3.26 | 3.27 | 3.46 | 3.95 | 3.40 | 3.66 | 3.53 | 3.73 | 3.96 | 4.19 | 4.16 |
| Tb | 0.60 | 0.66 | 0.55 | 0.52 | 0.57 | 0.63 | 0.55 | 0.60 | 0.58 | 0.59 | 0.63 | 0.72 | 0.71 |
| Dy | 3.45 | 3.85 | 3.11 | 2.84 | 3.26 | 3.72 | 3.20 | 3.56 | 3.11 | 3.24 | 3.56 | 4.28 | 4.32 |
| Ho | 0.74 | 0.81 | 0.66 | 0.62 | 0.71 | 0.84 | 0.71 | 0.80 | 0.72 | 0.71 | 0.75 | 0.95 | 0.96 |
| Er | 2.17 | 2.39 | 2.00 | 1.80 | 2.24 | 2.62 | 2.18 | 2.53 | 1.97 | 2.03 | 2.02 | 2.97 | 3.00 |
| Tm | 0.35 | 0.38 | 0.33 | 0.26 | 0.38 | 0.44 | 0.37 | 0.43 | 0.32 | 0.33 | 0.36 | 0.51 | 0.51 |
| Yb | 2.44 | 2.69 | 2.21 | 1.97 | 2.79 | 3.21 | 2.65 | 3.10 | 2.07 | 2.16 | 2.21 | 3.71 | 3.76 |
| Lu | 0.41 | 0.44 | 0.37 | 0.32 | 0.49 | 0.54 | 0.45 | 0.51 | 0.34 | 0.36 | 0.37 | 0.66 | 0.66 |
| Y | 19.73 | 21.43 | 17.37 | 18.10 | 19.86 | 23.07 | 25.77 | 22.58 | 19.60 | 20.50 | 21.10 | 25.85 | 26.43 |
| Σree | 116.07 | 115.30 | 95.54 | 108.16 | 118.44 | 130.96 | 113.70 | 122.18 | 108.26 | 124.93 | 123.87 | 130.02 | 137.27 |
| LREE | 102.32 | 100.09 | 83.05 | 96.56 | 104.55 | 115.03 | 100.20 | 107.00 | 95.62 | 111.78 | 110.01 | 112.03 | 119.19 |
| HREE | 13.75 | 15.21 | 12.49 | 11.60 | 13.89 | 15.93 | 13.50 | 15.18 | 12.64 | 13.15 | 13.86 | 18.00 | 18.08 |
| L/HREE | 7.44 | 6.58 | 6.65 | 8.32 | 7.53 | 7.22 | 7.42 | 7.05 | 7.56 | 8.50 | 7.94 | 6.22 | 6.59 |
| $La_N/Yb_N$ | 8.35 | 5.93 | 6.04 | 7.65 | 6.06 | 5.90 | 6.20 | 5.67 | 7.42 | 7.41 | 7.73 | 5.12 | 7.00 |
| δEu | 1.16 | 1.14 | 1.14 | 0.97 | 1.15 | 1.12 | 1.16 | 1.13 | 0.88 | 0.87 | 0.84 | 1.08 | 1.09 |
| δCe | 0.83 | 0.93 | 0.93 | 1.00 | 0.97 | 0.96 | 0.96 | 0.95 | 0.97 | 1.24 | 1.11 | 0.90 | 0.72 |
| Rb | 34.11 | 29.28 | 24.08 | 46.77 | 72.60 | 52.43 | 63.40 | 62.13 | 27.56 | 35.12 | 42.99 | 34.82 | 32.28 |
| Ba | 70.95 | 52.34 | 80.64 | 75.69 | 100.76 | 81.11 | 97.72 | 94.82 | 48.08 | 35.91 | 53.80 | 46.52 | 53.86 |
| Th | 36.01 | 33.96 | 35.60 | 30.94 | 37.89 | 38.26 | 37.21 | 37.84 | 53.18 | 48.47 | 51.29 | 50.33 | 46.72 |
| U | 53.05 | 65.00 | 50.90 | 53.81 | 52.48 | 49.05 | 48.86 | 50.10 | 69.05 | 61.90 | 74.29 | 70.00 | 56.19 |
| K | 4.98 | 5.64 | 4.98 | 3.98 | 3.65 | 3.98 | 3.65 | 4.32 | 4.98 | 5.64 | 4.98 | 4.65 | 4.65 |
| Ta | 18.20 | 17.41 | 15.05 | 13.66 | 12.00 | 12.12 | 11.78 | 12.29 | 15.37 | 12.68 | 21.71 | 13.66 | 12.73 |
| Nb | 9.85 | 10.15 | 9.96 | 9.54 | 7.78 | 8.26 | 8.14 | 8.35 | 9.99 | 9.23 | 11.77 | 10.49 | 10.34 |
| La | 41.28 | 32.31 | 27.07 | 30.57 | 34.31 | 38.33 | 33.29 | 35.63 | 31.15 | 32.46 | 34.64 | 38.53 | 53.30 |
| Ce | 22.79 | 23.50 | 19.68 | 24.45 | 25.86 | 28.32 | 24.68 | 26.21 | 23.61 | 31.66 | 29.46 | 26.53 | 24.79 |
| Sr | 41.62 | 41.69 | 41.43 | 40.38 | 42.60 | 46.70 | 44.76 | 38.61 | 26.54 | 30.14 | 31.09 | 32.21 | 28.96 |
| Nd | 16.45 | 17.75 | 14.48 | 16.03 | 17.43 | 19.13 | 16.68 | 17.87 | 15.95 | 16.40 | 16.40 | 18.94 | 19.03 |
| *P* | 166.29 | 170.88 | 170.88 | 170.42 | 144.24 | 148.83 | 135.51 | 162.62 | 158.48 | 176.40 | 165.83 | 151.13 | 152.97 |
| Hf | 10.53 | 10.95 | 10.53 | 21.10 | 12.54 | 12.28 | 12.50 | 12.32 | 19.45 | 20.03 | 19.35 | 13.50 | 13.34 |
| Zr | 9.64 | 10.00 | 9.77 | 13.93 | 12.40 | 12.30 | 12.38 | 12.29 | 14.64 | 14.64 | 15.09 | 13.29 | 13.08 |
| Sm | 10.40 | 11.25 | 9.03 | 8.83 | 9.69 | 10.48 | 9.18 | 9.94 | 9.82 | 9.95 | 10.92 | 11.33 | 11.29 |
| Ti | 1.29 | 1.29 | 1.29 | 1.34 | 1.06 | 1.01 | 1.06 | 1.01 | 1.75 | 1.80 | 1.66 | 1.66 | 1.34 |
| Y | 4.34 | 4.71 | 3.82 | 3.98 | 4.36 | 5.07 | 5.66 | 4.96 | 4.31 | 4.51 | 4.64 | 5.68 | 5.81 |
| Yb | 4.95 | 5.45 | 4.48 | 4.00 | 5.66 | 6.50 | 5.37 | 6.29 | 4.20 | 4.38 | 4.48 | 7.53 | 7.62 |
| Lu | 5.53 | 5.97 | 5.03 | 4.32 | 6.55 | 7.24 | 6.12 | 6.89 | 4.59 | 4.86 | 5.00 | 8.89 | 8.92 |

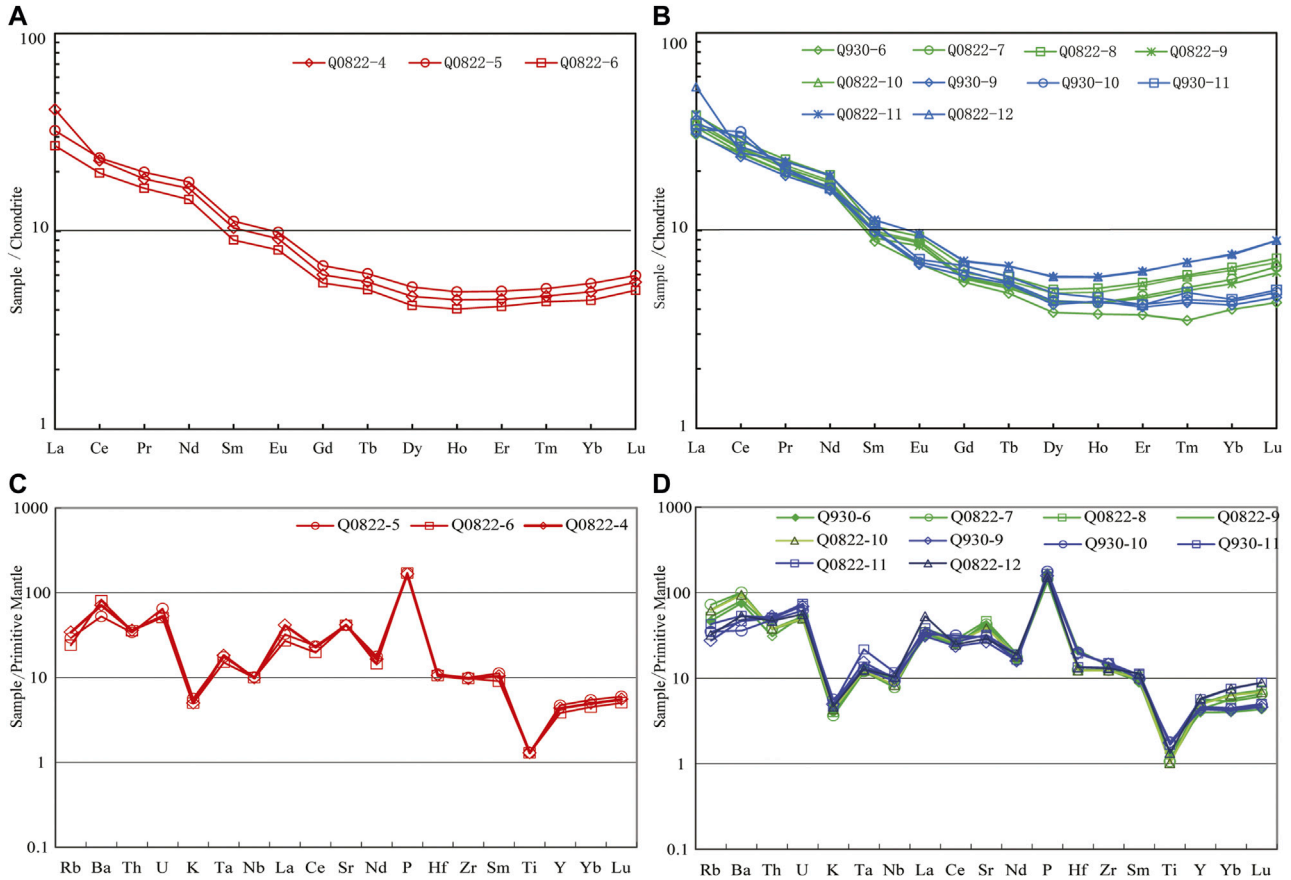


**FIGURE 9 |** Normalized REE distribution curves of chondrites from volcanic rocks and trace elements distribution curves of primitive mantle in the Xilekuduk area. **(A, C)** for Carboniferous stomatal andesites and **(B, D)** for Devonian dacites and andesites (chondrites data from Boynton (1984) and primitive mantle data from Sun and MCDonough (1989))

the Lower Carboniferous Jiangbastao Formation in the eastern part of the study area shows the characteristics of back arc basalts (Woodhead et al., 1993; Zhou et al., 2005). The cause of this phenomenon may be linked to the transitional environment and complex formation process; consequently, it is inferred that the diagenetic environment belongs to the early stage of plate collision.

On the Nb-Zr-Y tectonic environment discrimination diagram, Devonian and Carboniferous volcanic rock samples fall mainly in the volcanic arc basalt and the intraplate tholeiitic basalt area (**Figure 10A**), and all samples fall in island arc volcanic rocks on the Hf-Th-Ta diagram, showing the products of island arc environment (**Figure 10B**). This indicates that the diagenesis has certain transitional characteristics, and this may be related to the complex plate subduction and collision process.

## Relationship Between Volcanism and Iron and Molybdenum Mineralization

Magnetite is widely distributed in various types of deposits, such as the skarn type deposit, the Kiruna type deposit, the iocg type deposit, the magmatic type deposit, the BIF type deposit, and the porphyry type deposit (Dupuis and Beaudoin, 2011; Huberty et al., 2012; Hu et al., 2014). The content and variation range of major elements, trace elements, and rare earth elements of magnetite with different genesis differ: this can indicate different formation temperature, oxygen fugacity, sulfur fugacity, ore-forming material source, and tectonic environment, and so on (Pearce and Gale., 1977; Nadoll et al., 2012). Therefore, the mineral chemical characteristics of magnetite have certain typomorphic significance for distinguishing different types of ore deposits. For example, magnetite in skarn-type iron ore contains lower V and Ti, higher Ca, Al, and Mn contents than that in magmatic iron ore, and their REE characteristics are also obviously different (Frietsch and Perdahl, 1995; Dupuis and Beaudoin, 2011; Hu et al., 2014; Nadoll et al., 2014). The iron-bearing minerals in the Xilekuduk area are mainly magnetite. Through microscopic mineral research, it is found that MT1 magnetite is generally wrapped and metasomatized by MT2, and the contact boundary between them is clear, indicating that there are at least two stages of mineralization in this area. In recent years, some scholars have also identified two phases of magnetite in adjacent areas. For example, the Qiaoxiahala and Laoshankou iron–copper–gold

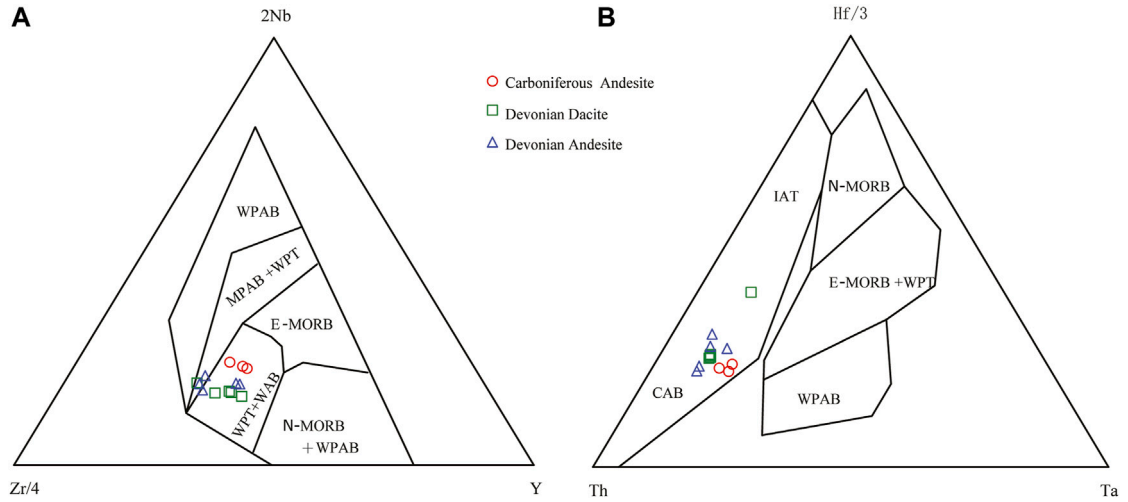


**FIGURE10 |** Tectonic environment discrimination diagram. **(A)** Diagrams of 2Nb-Zr/4-Y (Meschede, 1986) and **(B)** Hf/3-Th-Ta (Wood, 1979) of volcanic rocks in the Xilekuduk area. N-MORB: normal ridge basalt; E-MORB: enriched ridge basalt; WPAB: intraplate alkaline basalt; WPT: intraplate tholeiite; VAB: volcanic arc basalt; IAT: initial island arc tholeiite; and CAB: calc alkaline island arc volcanic rock.

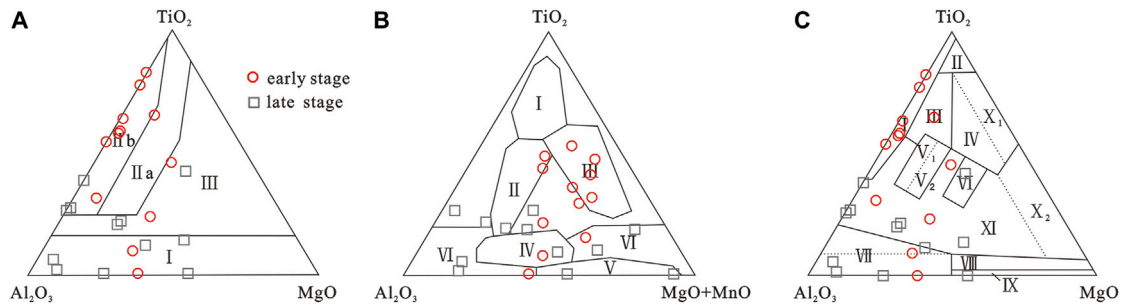


**FIGURE 11 |** Discrimination diagram of magnetite. **(A)** (Chen et al., 1987): I: sedimentary metamorphism-contact metasomatic magnetite; II a: ultrabasic–basic–neutral magmatic magnetite; II b: acid–alkaline magmatic magnetite. **(B)** (Xu and Shao, 1979): I: accessory mineral type; II: magmatic fused titanomagnetite type; III: volcanic rock type; IV: contact metasomatic type; V: skarn type; VI: sedimentary metamorphic type. **(C)** (Lin, 1982):I: granite area (acid magmatic pegmatite); II: basalt area (tholeiite, etc.); III: gabbro area (gabbro peridotite, monzonite, and anorthosite—accessory minerals and iron ore); IV: peridotite area (peridotite, peridotite, pyroxene, and other accessory minerals and iron ore); V1: amphibolite area (including clinopyroxenite); V2: diorite area; VI: kimberlite area; VII: hydrothermal type and calc skarn type (mainly plutonic hydrothermal type above dotted line, hydrothermal type and calc skarn type below); VIII: hydrothermal type and magnesium skarn type (plutonic hydrothermal type, part of hydrothermal metasomatism; magnesium skarn type); IX: sedimentary metamorphism and hydrothermal superimposition type; X: carbonate rock area (×1 is related to ultrabasic rocks, X2 is related to wall rock replacement); XI: transitional area.

deposits in the northern margin of Junggar, Xinjiang, were divided into two phases of magnetite, and it was noted that "dissolution reprecipitation" may have occurred in the mineralization process (Shang et al., 2017). The EPMA data of two typical magnetite samples (to be published in another article) show that MT1 magnetite has higher Ti and V and lower Ca, Al, Cr than MT2 magnetite. In the genetic diagram of $TiO_2$-$Al_2O_3$-MgO (**Figure 11A**), most of the early crystallized magnetites fall in the acid–alkaline magmatic magnetite region. The magnetite crystallized in the late stage is dispersed, and some of them fall in the area of sedimentary metamorphism-contact metasomatism. In the genetic diagram of $TiO_2$-$Al_2O_3$-MgO+ MnO genetic diagram (**Figure 11B**), magnetite crystallized in the early stage mainly falls in the volcanic rock type and the magmatic melt separated titanomagnetite type area. The magnetite crystallized in the late stage mainly occurs in contact metasomatic and skarn type areas. In the genetic diagram of $TiO_2$-$Al_2O_3$-MgO (**Figure 11C**), most of the early crystallized magnetites fall in the granite area (acidic magmatic pegmatite). The magnetite crystallized in the late stage mainly occurs in hydrothermal and calc skarn type areas. Therefore, the early crystallized magnetite MT1 is mostly of magmatic origin, while the late crystallized magnetite MT2 shows the characteristics of hydrothermal origin. This further confirms the existence of at least two stages of mineralization of magnetite. According to the banded occurrence characteristics of MT1 magnetite and the occurrence along with volcanic rocks in the Middle Devonian, it is inferred that the formation of MT1 magnetite is related to the

eruption and deposition of Devonian volcanoes (375–386 Ma). However, MT2 magnetite occurs in the form of magnetite quartz vein. Microscopically, it can be observed that MT2 magnetite is metasomatized by molybdenite and pyrite, which has hydrothermal characteristics. This may be similar to the "dissolution–reprecipitation" of magnetite in the surrounding the Qiaoxiahala and Laoshankou iron–copper–gold deposits. The relationship between magnetite and molybdenite in this stage is relatively close. Combined with the porphyry molybdenum metallogenic event in the ore district, it is speculated that MT2 magnetite may be related to porphyry molybdenum mineralization.

According to regional data, the study area experienced plate subduction, collision, and post-collision regional tectonic events in the late Paleozoic (Wang et al., 2006; Cai et al., 2011; Xiao and Santosh, 2014), accompanied by strong volcanism, such as volcanic eruption, eruption, and subvolcanism (Liu, 2001). According to the two stages of Late Paleozoic volcanic rock formation in the Xilekuduk area, the coupling relationship between two stages of volcanism and iron and molybdenum mineralization is sorted out:

In the early Devonian, the Junggar plate began to subduction northward and was in the tectonic environment of the plate margin. Volcanic rocks transited from tholeiitic (low-potassium) series to calc-alkaline series and then to high-potassium series of dacite, indicating that the island arc experienced the evolution process from early stage to mature stage. There are a large number of andesite dacite assemblages in the Xilekuduk area. The ages of these volcanic rock assemblages are between 375 and 385 Ma, showing typical island arc magmatic characteristics. During the intermittent period of volcanic eruption, the magmatic fluid rich in iron and copper first crystallized and precipitated between the layers of volcanic rocks, or interposed in the fissures of volcanic rocks, forming magnetite ore bodies mainly in strip and vein (Wilkinson, 2013), and a large number of banded and vein magnetite (MT1) were developed. With the crystallization differentiation of magma and the precipitation of copper element, the high background value of copper in volcanic rocks of the Beitashan Formation is formed. The Cu content of basalt is $95 \times 10^{-6}$–$25 \times 10^{-6}$, which is about 4 times of the Clark value of crust and that of andesite is $20 \times 10^{-6}$, which is roughly equivalent to the Clark value of crust, which provides material source for the formation of later copper deposits (Yang et al., 2010). In the Qiaoxiahara iron–copper–gold deposit on the northern side of the study area, iron ore body mainly occurs in the basalt-andesite volcanic rock of the Beitashan Formation of the Middle Devonian, which is derived from the early intermediate-basic volcanism (Ying, 2007). Therefore, the basalt andesite formation in the Xilekuduk area is an important iron-bearing area.

In the Early Carboniferous, the Junggar plate continued to subduction to form the Devonian–Early Carboniferous back arc ocean basin (Li, 2009). Volcanism in this stage was mainly subvolcanic facies, which was composed of intermediate–intermediate acid hypabyssal and ultrahypabyssal intrusive facies igneous rocks with different depths. The diagenetic age was concentrated in 340–318 Ma. Basaltic andesite porphyrite xenoliths are distributed in the granodiorite in the Xilekuduk area, suggesting that the source of crust mantle mixing of acid rock mass: the upper mantle material upwelling of asthenosphere induces the melting of lower crust material, and the mantle-derived magma rises and mixes with the crust source material, resulting in large-scale magma mixing (Wang et al., 2015), forming ore-bearing magma. Subsequently, the ore-bearing magma intruded and emplaced along the extensional structure, metasomatized the Devonian overflow andesite-sedimentary carbonate formation, forming a skarn belt. At the same time, a large amount of magmatic segregation formed a small amount of magnetite quartz veins (MT2), superimposed or wrapped early stratiform magnetite ore (MT1). With the gradual evolution of fluid, a large amount of Cu-Mo precipitates to form the Xilekuduk porphyry Cu-Mo deposit.

Volcanism and Fe-Cu-Mo mineralization in this area, therefore, bear the characteristics of multistage superimposed mineralization. The andesite–dacite formation in the Middle Devonian is closely related to the formation of early-stage magnetite, and the Early Carboniferous homologous heterogeneous volcanic rock formation, such as basaltic andesite-diorite-granite porphyry, is closely related to the porphyry copper mineralization and late-stage magnetite.

## CONCLUSION

1) The diagenetic age of dacite is 375.2 ± 2.9 Ma and that of andesite is 386.5 ± 3.0 Ma, which indicates that the volcanic rock was formed in the Middle Devonian, and the diagenetic age of stomatal andesite is 317.9 ± 2.9 Ma, it was formed in the Late Carboniferous.
2) The Devonian volcanic rock assemblage is composed of andesite and dacite. The content of $TiO_2$ varies from 0.34 to 0.35% and 0.42–0.47%, respectively. It belongs to the high-K calc-alkaline series, enriched in LREE, enriched in large ion lithophile elements Th, Rb, Ba, and K, and relatively depleted in HFSEs Nb, Ta, and Ti. The Carboniferous volcanic rocks are mainly stomatal andesite. The REE standard distribution pattern belongs to LREE enrichment type. The large ion lithophile elements Rb, Ba, and K are strongly enriched. The HFSEs Nb, Ta, and Ti are relatively depleted. The contents of $TiO_2$ and V are 0.94–0.97% and $178–183\times10^{-6}$, which are higher than those of island arc basalts. They are characterized by transitional diagenetic environment and are close to the stage of plate collision.
3) There are two periods of magnetite in the ore district. The stratiform magnetite ore MT1 produced along the early strata is mostly of magmatic origin. It is inferred that its formation is related to the eruption and deposition of Devonian volcano (375–386 Ma), while the magnetite MT2 of late magnetite quartz vein shows the characteristics of hydrothermal mineral, indicating the metal minerals precipitation in the early stage of the

mineralization of the Carboniferous (317.1 ± 2.9 ma) porphyry copper molybdenum deposit. Therefore, the volcanism and Fe-Cu-Mo mineralization in this area have the characteristics of multistage superimposed mineralization.

## DATA AVAILABILITY STATEMENT

The original contributions presented in the study are included in the article/Supplementary Material, further inquiries can be directed to the corresponding author.

## AUTHOR CONTRIBUTIONS

XW: wrote the paper and performed data treatment; HW: formulated the scientific problem, participated in writing the manuscript, and revised paper; ZL: provided natural samples and edited paper format; ZW: organized the research team and guided the study; DL: conducted the experiment; QM and XL: funding. All authors have read and agreed to the published version of the manuscript.

## FUNDING

This research was funded by the Natural Science Foundation of Hebei Province, Grant No. D2020403019; Science and Technology Research Project of University, Hebei Province, Grant No. ZD2020134; S&T Program of Hebei, Grant No. 19224205D; National Natural Science Foundation, Grant No. 41702165; the National Key R&D Program of China, Grant No. 2017YFC0601201 and 2017YFC0601204.

## ACKNOWLEDGMENTS

We are grateful to reviewers for helpful comments and suggestions.

## REFERENCES

Ablimit, E. (2017). *Genesis of Ore Forming Rocks in Xilekudouke Mo Deposit and Implication for Regional Mineralization [dissertation/doctor's Thesis]*. [Beijing: China University of Geosciences].

Andersen, T. (2002). Correction of Common Lead in U-Pb Analyses that Do Not Report 204Pb. *Chem. Geology.* 192 (1–2), 59–79. doi:10.1016/s0009-2541(02)00195-x

Boynton, W. V. (1984). "Cosmochemistry of the Rare Earth Elements:Meteorite Studies," in *Rare Earth Element Geochemistry*. Editor Henderson (New York: Elservier), Vol. 2, 63–114.

Cai, K., Sun, M., Yuan, C., Long, X., and Xiao, W. (2011). Geological Framework and Paleozoic Tectonic History of the Chinese Altai, NW China: a Review. *Russ. Geology. Geophys.* 52, 1619–1633. doi:10.1016/j.rgg.2011.11.014

Chen, G. Y., Sun, D. S., Yin, H. A., and Davidson, J. P. (1987). *Genetic Mineralogy and Prospecting Mineralogy1996*. in *Deciphering Mantle and Crustal Signatures in Subduction Zone Magmatism. Subduction Top to Bottom* (ChongqingWashington D. C: Chongqing Publishing PressGeophysical Monograph, Amercian Geophysical Union), 251–262.

Courfu, F., Hanchar, J. M., and Hoskin, P. W. O. (2003). Atlas of Zircon Textures. *Rev. Mineralogy Geochem.* 53, 469– 500. doi:10.2113/0530469

Deng, J. F., Luo, Z. H., Su, S. G., Mo, X. X., Ding, B. S., Lai, X. Y., et al. (2009). *Petrogenesis of Tectonics Environment and Metallogenesis*. Beijing: Geological Publishing Press. doi:10.1061/41039(345)179

Ding, R. F., You, J., and Li, C. X. (2011). Selection and Evaluation of Xilekuduke Cu–Mo–Au Prospecting Target in Xinjiang. *Mineral. Exploration* 2 (6), 740–748.

Dupuis, C., and Beaudoin, G. (2011). Discriminant Diagrams for Iron Oxide Trace Element Fingerprinting of Mineral Deposit Types. *Miner. Deposita.* 46, 319–335. doi:10.1007/s00126-011-0334-y

Frietsch, R., and Perdahl, J.-A. (1995). Rare Earth Elements in Apatite and Magnetite in Kiruna-type Iron Ores and Some Other Iron Ore Types. *Ore Geology. Rev.* 9 (6), 489–510. doi:10.1016/0169-1368(94)00015-g

Harris, N. B. W., Marzouki, F. M. H., and Ali, S. (1986). The Jabel Sayid Complex, Arabian Shield: Geochemical Constraints on the Origin of Peralkaline and Related Granites. *J. Geol. Soc.* 143, 287295. doi:10.1144/gsjgs.143.2.0287

Hu, H., Li, J. W., and Lentz, D. (2014). Dissolution-reprecipitation Process of Magnetite from the Chengchao Iron Deposit: Insights into Ore Genesis and Implication for in– Situ Chemical Analysis of Magnetite. *Ore Geology. Rev.* 57, 393–405. doi:10.1016/j.oregeorev.2013.07.008

Huberty, J. M. (2012). Silician Magnetite from the Dales Gorge Member of the Brockman Iron Formation, Hamersley Group, Western Australia. *Am. Mineral.* 97, 26–37. doi:10.2138/am.2012.3864

Irvine, T. N., and Baragar, V. R. (1971). Aguidetothechemical Classificationof Thevolcanicrocks. *Can. J. Earth. Sci.* 8, 523–548. doi:10.1139/e71-055

Li, C. M. (2009). A Review on the Minerageny and Situmicroanalytical Dating Techniques of Zircons. *Geol. Surv. Reasearch* 33 (3), 161–174. doi:10.1007/978-3-642-01053-8_70

Li, W. Y., Dong, F. C., Zhang, Z. W., Tan, W. J., Jiang, H. B., and Xiao, C. Y. (2015). Major Progress and Achievements in Study of the Metallogenic Prospect and Prospecting Deployment of Mineral Resources in Northwest China. *Geol. Surv. China* 2 (1), 19–24. doi:10.19388/j.zgdzdc.2015.01.004

Lin, S. Z. (1982). Discussion on the Mineral Chemistry, Genesis and Evolution of Magnetite. *J. Mineralogy* (3), 166– 174. doi:10.16461/j.cnki.1000-4734.1982.03.002

Liu, J. Y. (2001). Continental Volcanic and Gold-Coper Metallogensis in East Junggar, Xinjiang. *Geotectonics and metallogeny* 25 (4), 1434–1438. doi:10.16539/j.ddgzyckx.2001.04.010

Long, L. L., Wang, J. B., Wang, Y. W., Wang, L. J., Liao, Z., Zhao, L. T., et al. (2014). Characteristics of REE Composition and Trace Element of the Pyrites from the Xilekuduke Cu-Mo Deposit in Xinjiang. *Mineral. Exploration* 5 (02), 169–177.

Long, L. L., Wang, J. B., Wang, Y. W., Wang, L. J., Wang, S. L., and Pu, K. X. (2009). Geochronology and Geochemistry of the Ore–Bearing Porphyry in Xilekuduke Cu–Mo Deposit, Fuyun Area, Xinjiang, China. *Geol. Bull. China* 28 (12), 18401851

Long, L. L., Wang, Y. W., Du, A. D., Wang, J. B., Wang, L. J., Wang, S. L., et al. (2011). Molybdenite Re–os Age of Xilekuduke Cu–Mo Deposit in Xinjiang and its Geological Significance. *Mineral. Deposits* 30 (4), 635–644. doi:10.16111/j.0258-7106.2011.04.004

Meschede, M. (1986). A Method of Discriminating between Different Types of Mid–ocean Ridge Basalts and Continental Tholeiites with the Nb–Zr–Y Diagram. *Chem. Geol.* 56 (3/4), 207–218. doi:10.1016/0009-2541(86)90004-5

Nadoll, P., Angerer, T., and Mauk, J. L, (2014). The Chemistry of Hydrothermal Magnetite: A Review. *Ore Geology. Rev.* 61, 1–32. doi:10.1016/j.oregeorev.2013.12.013

Nadoll, P., Mauk, J. L., and Hayes, T. S. (2012). Geochemistry of Magnetite from Hydrothermal Ore Deposits and Host Rocks of the Mesoproterozoic Belt Supergroup, United States. *Econ. Geology.* 107, 1275–1292. doi:10.2113/econgeo.107.6.1275

Othman, B. D., White, W. M., and Patchett, J. (1989). The Geochemistry of Marine Sediment, Island Arc Magma Genesis and Crust-Mantle Recycling. *Earth Planet. Sci. Lett.* 94, 1–24. doi:10.1016/0012-821x(89)90079-4

Pearce, J., and Gale, G. (1977). Identification of Ore-Deposition Environment from Trace–Element Geochemistry of Associated Igneous Host Rocks. *Geol. Soc. Lond. Spec. Publications* 7 (1), 14–24. doi:10.1144/gsl.sp.1977.007.01.03

Sengör, A. M. C., Natalin, B. A., and Burtman, V. S. (1993). Evolution of the Altaid Tectonic Collage and Paleozoic Crustal Growth in Eurasia. *Nature* 364, 299–307.

Shang, H. J., Li, Q., Yu, X. B., and Li, Y. (2017). Analysis of Magnetite Composition and Geological Characteristics of Qiaoxiahala and Laoshankou Fe-Cu-Au Deposits in the Northern Junnggar, Xinjiang. *Xinjiang Geology*. 35 (1), 43–49.

Sun, S. S., and McDonough, W. F. (1989). "Chemical and Isotopic Systematics of Oceanic Basalts: Implications for Mantle Composition and Processes,". *Magmatism in Oceanic Basins*. Editors A. D. Saunders and M. J. Norry (London: Spec. Publ. Geol. Soc. Lond.), 42, 313–345. doi:10.1144/gsl.sp.1989.042.01.19

Wang, J. B., and Xu, X. (2006). Post–collisional Tectonic Evolution and Metallogenesis in Northern Xinjiang, China. *ACta geologica sinica* 80 (1), 23–31.

Wang, Y. W., Wang, J. B., Long, L. L., Ding, R. F., Shi, Y., and Zhao, L. T. (2015). The Early Carboniferous Gold-Copper-Molybdenum Mineralization Events in the Northern Margin of Junggar BasinXinjiang: Geochronological Evidence. *Acta Petrologica Sinica* 31 (5), 14481460

Wei, X. F., Pan, D., Yuan, J., Liao, Z., Lu, X. Q., Shan, L. H., et al. (2019). Zircon U-Pb Age of Biotite Granite and 39Ar/40Ar Age of Sericite from Aketasi Gold Deposit in Xinjiang, and Their Geological Significance. *Mineral. Deposits* 38 (2), 251–260. doi:10.16111/j.0258-7106.2019.02.002

Wilkinson, J. (2013). Triggers Fou the Formation of Porphyry Ore Deposits in Magmaticaecs. *Nat. Geosci.* 6 (11), 917–925. doi:10.1038/ngeo1940

Windley, B. F., Alexeiev, D., Xiao, W., Kroner, A., and Badarch, G. (2007). Tectonic Models for Accretion of the Central Asian Orogenic Belt. *J. Geol. Soc. Lond.* 164, 31–47. doi:10.1144/0016-76492006-022

Wood, D. A. (1979). A Variably Veined Suboceanic Upper Mantle: Genetic Significance for Mid–ocean Ridge Basalts from Geochemical Evidence. *Geology* 7 (10), 499–503. doi:10.1130/0091-7613(1979)7<499:avvsum>2.0.co;2

Woodhead, J. D., Eggins, S. M., and Gamble, J.(1993). High Field Strength and Transition Element Systematics in Island Arc and Back Arc Basin Basalts: Evidence for Multi-phase Melt Extraction and a Depleted Mantle Wedge. *Earth Planet. Sci.Lett.* 114, 4 91–50.doi:10.1016/0012-821x(93)90078-n

Xiao, W. J., and Santosh, M. (2014). The Western Central Asian Orogenic Belt: A Window to Accretionary Orogenesis and Continental Growth. *Gondwana Res.* 25 (4), 1429–1444. doi:10.1016/j.gr.2014.01.008

Xu, G. F., and Shao, L. J. (1979). The Typomorphic Characteristics of Magnetite and its Practical Significance. *Geology. exploration* 3, 30–37.

Yang, F. Q., Chai, F. M., Zhang, Z. X., Geng, X. X., and Li, Q. (2014). Zircon U–Pb Geochronology, Geochemistry, and Sr–Nd–Hf Isotopes of Granitoids in the Yulekenhalasu Copper Ore District, Northern Junggar, China: Petrogenesis and Tectonic Implications. *Lithos* 190–191, 85–103. doi:10.1016/j.lithos.2013.12.003

Yang, F. Q., Mao, J. W., Bierlein, F. P., Pirajno, F., Zhao, C. S., Ye, H. S., et al. (2009). A Review of the Geological Characteristics and Geodynamic Mechanisms of Late Paleozoic Epithermal Gold Deposits in North Xinjiang, China. *Ore Geology. Rev.* 35, 217–234. doi:10.1016/j.oregeorev.2008.09.003

Yang, F. Q., Mao, J. W., Pirajno, F., Yan, S. H., Liu, G. R., Zhou, G., et al. (2012). A Review of the Geological Characteristics and Geodynamic Setting of Late Paleozoic Porphyry Copper Deposits in the Junggar Region, Xinjiang Uygur Autonomous Region, Northwest China. *J. Asian Earth Sci.* 49, 80–98. doi:10.1016/j.jseaes.2011.11.024

Yang, F. Q., Yan, S. H., Liu, G. R., Zhou, G., Zhang, Z. X., Liu, F., et al. (2010). Geological Characteristics and Metallogenesis of Porphyry Copper Deposits in Junggar, Xinjiang. *Mineral. Deposits* 29 (6), 956– 971. doi:10.16111/j.0258-7106.2010.06.012

Ying, L. J. (2007). *Geology,Geochemistry and Discussion on the Origin of the Qiaoxiahala Fe-Cu-Au Deposit in Xinjiang*. [Beijing]: Chinese Academy of Geological Sciences[dissertation/master's Thesis].

You, J., Hong, T., Wu, C., Ding, R. F., and Xu, X. W.(2016). Characteristics of Magmatic Activity in the Xilekuduke Mo-Cu Ore District, Fuyun County, *Xinjiang, and its Constrains on Regional Tectonic Evolution in Late-Post Collisional Stages*. 32(5), 1262–1282.

Yuan, H. L., Wu, F. Y., Gao, S., Liu, X. M., Xu, P., and Sun, D. Y. (2003). Precise Determinations of U–Pb Age and Rare Earth Element Concentrations of Zircons from Cenozoic Intrusions in Norther China by Laser Ablation ICP–Ms. *Chin. Sci. Bull.* 48 (22), 4211–2421.

Zhang, H. X., Niu, H. C., and Sato, H. (2005). Late Paleozoic Adakites and Nb-Enriched Basalts from Northern Xinjiang, NW China: Evidence for the Southward Subduction of the Pale-Asian Oceanic Plate. *The Isl. Arc* 14 (1), 55–68. doi:10.1111/j.1440-1738.2004.00457.x

Zhang, H. X., Niu, H. C., Shi, X. M., Ma, L., and Yu, X. Y. (2008). Late Paleozoic Tectonic Evolution and Polymetallic Ore–Forming Processes in Southern Altay and Northern Junggar. *Minera deposits* 27 (5), 596–600.

Zhang, Z. C., Yan, S. H., Chen, B. L., Zhou, G., He, Y. K., Chai, F. M., et al. (2006). SHRIMP Zicron U-Pb Dating for Subducting–Related Granitic Rocks in the Northern Part of East Junggar, Xinjiang. *Chin. Sci. Bull.* 51 (13), 1565–1574. doi:10.1007/s11434-008-0952-7

Zhou, G., Zhang, Z. C., Yang, W. P., Gu, G. Z., Zhang, X. L., Luo, S. B., et al. (2005). Metabasic Rock on the South Side of Mayin'ebo Fault in the South Margin of Altay Mountains, Xin Jiang, and its Geological Implications. *Earth Science-Journal China Univ. Geosciences* 30 (6), 738–747.

**Conflict of Interest:** XW was employed by the Zhongse Zijin geological exploration (Beijing) Co., Ltd., ZL was employed by the Sinotech Minerals Exploration Co., Ltd., and QM was employed by the Beijing Institute of mineral geology Co., Ltd.

The remaining authors declare that the research was conducted in the absence of any commercial or financial relationships that could be construed as a potential conflict of interest.